crystals

MDPI

Article

Assessment of Inclusion Removal Ability in Refining Slags Containing Ce_2O_3

Jianqi Cao [1], Yao Li [1,2], Wanming Lin [1,3,*], Julong Che [4], Feng Zhou [5], Yunfang Tan [4], Dongliang Li [6], Jie Dang [7] and Chao Chen [1,*]

1 College of Materials Science and Engineering, Taiyuan University of Technology, Taiyuan 030024, China
2 State Key Laboratory of Advanced Metallurgy, University of Science and Technology Beijing, Beijing 100083, China
3 Department of New Energy and Materials Engineering, Shanxi Electronic Science and Technology Institute, Linfen 041075, China
4 The Third Geological Center Laboratory, China Metallurgical Geology Administration, Taiyuan 030027, China
5 Shanxi Taigang Stainless Steel Co., Ltd., Taiyuan 030030, China
6 Department of Chemistry & Chemical Engineering, Lvliang University, Lvliang 033001, China
7 College of Materials Science and Engineering, Chongqing University, Chongqing 400044, China
* Correspondence: linwanming@tyut.edu.cn (W.L.); chenchao@tyut.edu.cn (C.C.); Tel.: +86-155-3657-5503 (C.C.)

Abstract: The elimination of inclusions in steelmaking processes has been widely studied. The removal of inclusions by slags containing the rare earth oxide Ce_2O_3 are studied using an integrated numerical model. The integrated model involves the inclusion motion model, interfacial tension calculation model, surface tension calculation model of slag, and the mass action concentration model, based on ion and molecule coexistence theory. The motion behaviors of both solid Al_2O_3 inclusions and 50%wtAl_2O_3–50%wtCaO liquid inclusions of varied sizes at CaO-Ce_2O_3-SiO_2-Al_2O_3(-MgO) slag systems are evaluated. The results show that it is more difficult to remove the inclusions with smaller sizes and in slag with a higher viscosity. Liquid inclusions are more difficult to remove than solid inclusions. It is found that the CaO-Ce_2O_3-SiO_2-Al_2O_3-MgO refining slag shows a better ability to remove Al_2O_3 inclusions than that of the CaO-SiO_2-Al_2O_3-MgO slag. The reason for this is that the addition of the rare earth oxide Ce_2O_3 can decrease the viscosity of slags, as well as improving the wetting effects of slags on Al_2O_3 inclusions. For two slags systems, the CaO-Ce_2O_3-SiO_2-Al_2O_3-MgO slag system shows a better ability to remove Al_2O_3 inclusions than the CaO-Ce_2O_3-SiO_2-Al_2O_3 slag system. The addition of 5% to 8% Ce_2O_3 in a CaO-SiO_2-Al_2O_3-MgO slag is an optimized case for industrial applications.

Keywords: inclusions; removal of inclusions; refining slag; rare earth oxide contained slag; ion and molecule coexistence theory; numerical model

check for updates

Citation: Cao, J.; Li, Y.; Lin, W.; Che, J.; Zhou, F.; Tan, Y.; Li, D.; Dang, J.; Chen, C. Assessment of Inclusion Removal Ability in Refining Slags Containing Ce_2O_3. *Crystals* **2023**, *13*, 202. https://doi.org/10.3390/cryst13020202

Academic Editor: Cyril Cayron

Received: 21 November 2022
Revised: 17 January 2023
Accepted: 17 January 2023
Published: 23 January 2023

1. Introduction

Non-metallic inclusions are harmful to steel product quality [1–3], and they also influence the steelmaking process via clogging of the nozzles [4–6]. A great number of studies have focused on the analysis of inclusions during the whole steelmaking process [7–15]. Meanwhile, the inclusion formation and control in a steelmaking unit, for example, a ladle furnace [16–18], vacuum degassing [19–22], Ruhrstahl–Heraeus [23–27], and tundish [28–31] have also been widely studied.

Absorption by slag [32–34] and adhesion to refractories [35] are two common ways to remove inclusions. Adherence to rising bubbles is a good method for the floatation of inclusions. The process of inclusion absorption by the top slag can be divided into four steps [36]: (1) inclusions are transported to the turbulent boundary layer of the steel–slag interface; (2) inclusions transport through the boundary layer to the steel–slag interface; (3) inclusions separate to the slag; and (4) inclusions are dissolved in the slag phase.

For step (1), a great number of studies have focused on the nucleation, motion, collision, and transport of inclusions in secondary refining units by using fundamental water models [37–42], mathematical models [43–47], and Computational Fluid Dynamics (CFD) models [48–66]. Both the Eulerian approach (the statistical evaluation of inclusion species) and the Lagrangian approach (the evaluation of particles) were used in the models. However, as reviewed by C. Chen et al. [66], steps (2)–(4) of the removal of inclusions were neglected in most CFD studies. This is challenging as it is a combination of all the steps. The set-up of inclusion removal in slag is according to the Stokes rising velocity in most Eulerian approaches, following the work of Tacke and Ludwig [67]. In Lagrangian approaches, the inclusion particles were commonly treated as being fully absorbed by the slag once the particle touched the interface. A novel approach was developed [68] by considering a critical velocity condition to evaluate the trap or to reflect the conditions of inclusions. A more complicated approach was developed recently [69].

As mentioned above, step (1) can be modeled elaborately in the CFD models. One attempt was made to combine steps (1)–(2) in a CFD model [66,70]. It was found that the interface slip velocity has a greater influence on the removal of small-sized inclusions. Step (2), i.e., the deposition of inclusions at the boundary layer of steel–slag interface, is dominant and cannot be neglected for small inclusions. In contrast, the influence of the boundary layer on large-sized inclusions is negligible since the inclusions are likely to penetrate the boundary layers. Thus, steps (3) and (4) are considered to be key steps for the removal of inclusions in general descriptions [32].

The studies on step (3) could be dated back to a pioneer work by Nakajima and Okamura [71] in 1992. They developed a model for single solid spherical inclusion motion at the steel–slag interface. This model could be categorized into a Lagrangian approach, which was based on Newton's second law. The model has been continuously developed by introducing the turbulent burst theory to calculate the possibility of the re-entrainment of inclusions [72], by applying it to solid inclusions of other compositions [15,33,73] and liquid inclusions [74,75], by extending the model to different shapes of inclusions, such as octahedral and plate-like, etc. [76–78], by introducing the slag dissolution kinetics [79], by improving the theory of a slag film capture [80], and by applying it to a study on the water model of particles [81,82]. Recently, CFD models coupled flow–solid interaction [83,84] or the use of the dynamic overset grid technique [85] were developed to study the inclusion motion and separations. Furthermore, the motions of inclusions under a supergravity field were studied from a new perspective [86].

For step (4), inclusions dissolution in slags has been widely studied using experiments [34,87–94] and numerical models [79,95–98]. It worth mentioning that the oxide dissolution in slags have been studied using a novel in situ observation method [92,98]. In addition, phase field models have been developed to study the dissolution of inclusions [95–98]. Recently, a concept of the inclusion capacity of slag is put forward [94].

Typically, slag is formed in many processes [99–107]; for example, ironmaking, convertor steelmaking, refining, continuous casting, the electroslag remelting process, and ferroalloys production. The thermodynamic properties and physicochemical properties of many types of slags have been widely evaluated and modeled [108–114]. Typical refining slags are CaO-Al_2O_3-SiO_2 slag and CaO-SiO_2-Al_2O_3-MgO slag systems. The inclusions dissolution in two slag systems have been studied [90–92,115].

For rare earth (RE) oxides, it has been added in liquid steel, as mentioned, and reviewed by Hasegawa and Sakuma [116] in 1956. It is noted that the rare earth metal addition in liquid steel in ingot casting processes have been widely investigated in 1940–1970s [116–118]. The clogging of the submerged entry nozzles of RE oxide inclusions have hindered the application of RE element addition in steels in continuous casting routes [119]. Later, in the 1970s, the phase diagram of Al_2O_3-REO_X was systematically measured by Mizuno et al. [120,121]. An attempt on the activity measurement in steelmaking slags CaO-Al_2O_3-Ce_2O_3 was first performed by Ueda et al. [122]. The thermodynamic properties, including phase diagram [123–125], structure [126–128], the activity and mass action concentration [129–131];

and physicochemical properties, including the viscosity [127,128,131], melting point [132,133], and surface tension [134] of the slag were studied. According to the research results, the addition of rare earth oxides in refining slag can reduce the activity of Al_2O_3 in slag and increase the viscosity and the melting point of slag. Attempts were also made to evaluate the effects of rare earth oxides-containing slags on steel cleanliness [135], as well as the performance of the microalloying of rare earth elements in steels by reducing the rare earth oxides in slag [136,137]. The microalloying method may be an alternative way to add rare earth elements into steel. Specifically, the balance between the Ce_2O_3-containing refining slag and the molten steel-containing aluminum will lead to a small amount of cerium being dissolved into the molten steel. This rare earth element can perform a vital role in purifying, modifying, and micro-alloying steels [138], modifying the inclusions [139–142], refining the solidification structure [143], and improving the performance [144–146] of RE steels. The effects of rare earth elements on the modification of inclusions have been widely studied, both in lab experiments and within industrial scale production. The rare earth can react with O and S to form rare earth oxygen sulfide [139]. The sizes of inclusions are also decreased. However, the mechanism of inclusion absorbed by the rare earth oxide-containing slag is still unclear.

In this paper, the separation of inclusions to the rare earth oxide-containing slag are studied. The motion behaviors of both solid Al_2O_3 inclusions and the liquid inclusions of varied sizes at CaO-Ce_2O_3-SiO_2-Al_2O_3 and CaO-Ce_2O_3-SiO_2-Al_2O_3-MgO slag systems are evaluated using an integrated numerical model. The integrated model involves the inclusion motion model, the interfacial tension calculation model, the surface tension calculation model of slag, and the mass action concentration model, based on the ion and molecule coexistence theory. This paper is organized as follows: all the model descriptions, validations, and calculation process parameters are presented in Section 2. The results and discussions are presented in Section 3. The results can be used to predict the movement of inclusions at the steel–slag interface, with different overall wettabilities of the steel–slag-inclusion system. It will provide hints for the design of the refining slag composition, and an evaluation method of inclusion removal ability in the slags.

2. Modeling Methodology and Model Details

The studied CaO-Ce_2O_3-SiO_2-Al_2O_3 and CaO-Ce_2O_3-SiO_2-Al_2O_3-MgO slag systems are denoted as slag A and slag C, respectively. The scope and flow chart of the models are shown in Figure 1.

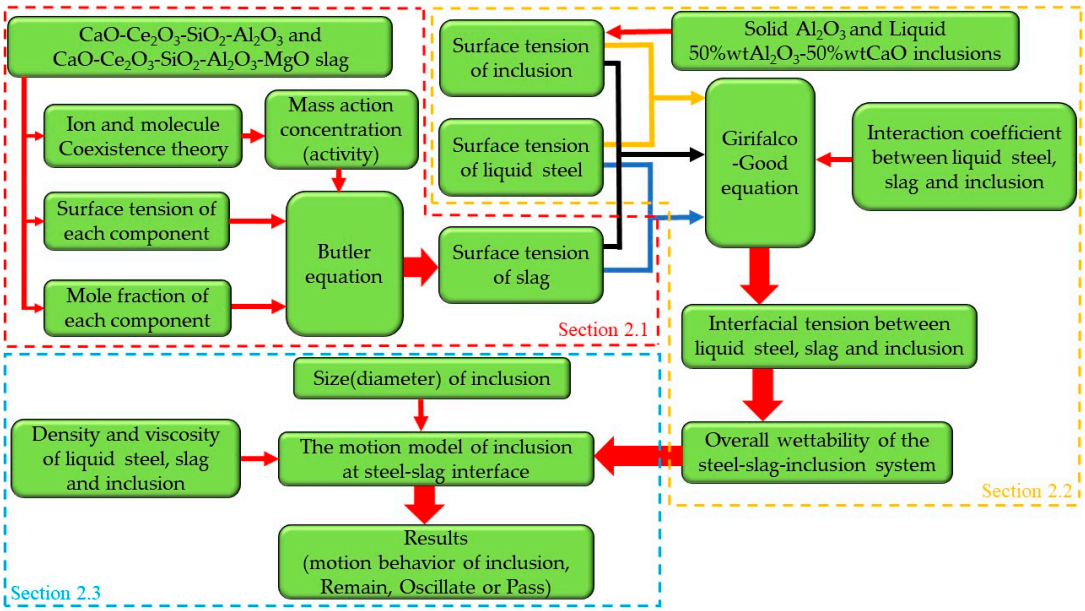

Figure 1. Flow chart of integrated calculation model of inclusion motion.

The inclusion motion model requires the input of the properties of slags and inclusions; for example, the density and viscosity of slags, and the overall wettability of the steel–slag-inclusion system. The density and viscosity data of the two slag systems are referred from [87,133]. The overall wettabilities of steel–slag inclusions require interfacial tension between each of the two components, i.e., the interfacial tension of steel–slag, steel–inclusion, and slag–inclusion. The estimation of the interfacial tension via the Girifalco-Good equation may further require the surface tension of steel, inclusion, and slag, respectively. Thereafter, the data of the inclusion and steel have been widely studied. The surface tension of rare earth oxide-containing slag is a challenging work. The estimation model using the Butler equation and the individual surface tension of the oxide component can be utilized. In the model, the molar fraction and the activity of the oxide component are required data. Alternatively, the mass action concentration (activity) of the oxide could be calculated using the well-known ion and molecule coexistence theory.

The previous analysis followed a sequence from the modeling strategy perspective. In this section, the inverse order of model descriptions will be presented. Specifically, the surface tension of slag will be described in Section 2.1. The ion and molecule coexistence theory, and the Butler equation-based model will be briefly introduced in Sections 2.1.1 and 2.1.2, respectively. The specific surface tension of the CaO-Ce_2O_3-SiO_2-Al_2O_3 and CaO-Ce_2O_3-SiO_2-Al_2O_3-MgO slag systems will be illustrated in Sections 2.1.3 and 2.1.4, respectively. Secondly, the interfacial tension of steel–inclusion, slag–inclusion, and steel–slag will be calculated in Sections 2.2.1–2.2.3, under Section 2.2. The yellow dotted line box in Figure 1 shows the calculation flow in Section 2.2, and the arrow indicates that the parameter value obtained in the previous step is substituted into the formula for the next step. For example, the yellow arrow indicates substituting the value of the surface tension of solid Al_2O_3 or liquid 50%wtAl_2O_3–50%wtCaO inclusion and the surface tension of liquid steel into the Girifalco-Good equation. The interfacial tension between liquid steel and inclusion can be calculated by substituting the determined value of the interaction coefficient at the same time. After this, the overall wettability of the steel–slag-inclusions is obtained. The inclusion motion model will be described in Section 2.3. The results of the motion behavior of the solid and liquid inclusions will be presented in the Results and Discussion sections. It should be noted that the overall studied 11 slag compositions are presented in Tables 1–4.

Table 1. The viscosities of CaO-Ce_2O_3-SiO_2-Al_2O_3 of different compositions at 1773 K (mass fraction).

Serial	CaO %wt	Al_2O_3 %wt	SiO_2 %wt	Ce_2O_3 %wt	Basicity C/A	Viscosity (Pa·s)
A1	54.64	30.36	10	5	1.8	0.416
A2	51.00	34.00	10	5	1.5	0.363
A3	46.36	38.64	10	5	1.2	0.398
A4	51.43	28.57	10	10	1.8	0.497
A5	48.21	26.79	10	15	1.8	0.289

Table 2. The mole fractions of studied CaO-Ce_2O_3-SiO_2-Al_2O_3 slag cases.

Serial	X_{CaO}	$X_{Al_2O_3}$	X_{SiO_2}	$X_{Ce_2O_3}$
A1	0.6705	0.2045	0.1145	0.0105
A2	0.6387	0.2338	0.1169	0.0107
A3	0.5962	0.2728	0.1200	0.0110
A4	0.6580	0.2007	0.1194	0.0218
A5	0.6444	0.1966	0.1248	0.0342

The studied composition and viscosity of the CaO-Ce_2O_3-SiO_2-Al_2O_3 slag system are listed in Table 1; the viscosity data are referred to from [133].

The composition of slag is converted to mole fraction and shown in Table 2.

The studied composition and viscosity of the CaO-Ce_2O_3-SiO_2-Al_2O_3-MgO slag system are listed in Table 3; the viscosity data are referred from [87,88].

The composition of slag is converted to mole fraction and shown in Table 4.

Table 3. Mass fraction composition and viscosity of CaO-Ce_2O_3-SiO_2-Al_2O_3-MgO slag system at 1823 K.

Serial	CaO %wt	Al_2O_3 %wt	SiO_2 %wt	MgO %wt	Ce_2O_3 %wt	Basicity C/A	Viscosity (Pa·s)
C0	48	37.5	4.5	10	0	1.27	0.495
C1	45	37.5	4.5	10	3	1.2	0.307
C2	46.2	36.3	4.5	10	3	1.27	0.374
C3	45	35.5	4.5	10	5	1.27	0.225
C4	43.4	34.1	4.5	10	8	1.27	0.265
C5	45	32.5	4.5	10	8	1.385	0.264

Table 4. The mole fraction of studied CaO-Ce_2O_3-SiO_2-Al_2O_3-MgO slag cases.

Serial	X_{CaO}	$X_{Al_2O_3}$	X_{SiO_2}	X_{MgO}	$X_{Ce_2O_3}$
C0	0.5531	0.2371	0.0484	0.1613	0
C1	0.5338	0.2442	0.0498	0.1661	0.0061
C2	0.5445	0.2349	0.0495	0.165	0.006
C3	0.5386	0.2333	0.0503	0.1676	0.0102
C4	0.5313	0.2292	0.0514	0.1714	0.0167
C5	0.5461	0.2165	0.051	0.1699	0.0166

2.1. Calculation Model of the Surface Tension of Slag

2.1.1. The Ion and Molecule Coexistence Theory

The ion and molecule coexistence theory of molten slag is based on the analysis of the structural units existing in molten slag. According to the equilibrium reaction equation and the equilibrium constant between the components, and from calculating the mass action concentration of each component, to determine the activity of each component in molten slag.

The ion and molecule coexistence theory describes the slag structure as [147]:

1. Slag is composed of various ions, compounds (molecules), and electrons. For the slag system studied in this paper, slag contains Ca^{2+}, O^{2-}, Ce^{2+}, Mg^{2+}, Al_2O_3, SiO_2, and aluminate and silicate generated by their mutual reactions.
2. The coexistence of ions and molecules is continuous in the slag system of any composition.
3. Dynamic equilibrium reactions are achieved between ions and molecules.
4. The chemical reaction in slag obeys the law of mass action.

It is considered that this theory can be extended from inside of the slag to the surface of slag, so that the surface tension of the slag can be calculated [148]. Recently, many scholars have used this theory to carry out theoretical calculation research, and the results are in good agreement with the experimental results [149–152].

2.1.2. The Butler Equation

The Butler equation proposes that the surface of the solution is regarded as the surface phase, and that the relationship between the surface tension and the thermodynamic parameters is deduced based on the assumption that the components in the surface phase and the components in the bulk phase are in thermodynamic equilibrium [153,154]. This model calculates the surface tension of slag based on the Butler equation, which can be expressed as:

$$\sigma = \sigma_i^0 + \frac{RT}{A_i} ln \frac{N_i^{Surf}}{N_i^{Bulk}} \quad (1)$$

where σ_i^0 is the surface tension of pure component i, R is a gas constant, T is the temperature, and N_i^{Surf} and N_i^{Bulk} are the mass action concentrations of component i in the surface phase and bulk phase, respectively. A_i is the surface area of the monolayer atoms of component i, which can be expressed as:

$$A_i = L \cdot N_A^{1/3} \cdot V_i^{2/3} \tag{2}$$

where L is the correction factor caused by the surface structure, which is related to the arrangement of monolayer atoms in the lattice. For a molten salt and ionic oxide mixture, it is usually set to 1.091. N_A is Avogadro's constant, $N_A = 6.02 \times 10^{23}$; V_i is the molar volume of component i.

Taking a multi-components slag system as an example, the calculation steps of the model are:

1. The mass action concentration N_i^{Bulk} of each component in a multi-components slag system are calculated by using the ion and molecule coexistence theory;
2. According to Equation (1), the expression of the mass action concentration N_i^{Surf} of each component on the surface of a multi-components slag system can be written;
3. For a combination of the surface tension and the molar volume data of each component, the equation $\sum N_i^{Surf} = 1$ and the expansion of the Butler equation, the mass action concentrations N_i^{Surf} of each component on the surface of a multi-components slag system are obtained;
4. The surface tension is acquired by solving the Butler equation.

2.1.3. Surface Tension Calculation of the CaO-Ce_2O_3-SiO_2-Al_2O_3 Slag System

(1) Mass Action Concentration Calculation of Each Component

Based on the ion and molecule coexistence theory and phase diagram, the CaO-Ce_2O_3-SiO_2-Al_2O_3 slag system was analyzed. At a refining temperature of 1773~1873 K, the slag contains three kinds of ions Ca^{2+}, O^{2-}, Ce^{2+}, two kinds of simple molecules, Al_2O_3 and SiO_2, and 13 kinds of complex molecules $CaO{\cdot}Al_2O_3$, $CaO{\cdot}2Al_2O_3$, $CaO{\cdot}6Al_2O_3$, $3CaO{\cdot}Al_2O_3$, $12CaO{\cdot}7Al_2O_3$, $CaSiO_3$, Ca_2SiO_4, Ca_3SiO_5, $Ce_2O_3{\cdot}Al_2O_3$, $Ce_2O_3{\cdot}11Al_2O_3$, $2CaO{\cdot}Al_2O_3{\cdot}SiO_2$, $CaO{\cdot}Al_2O_3{\cdot}2SiO_2$, and $3Al_2O_3{\cdot}2SiO_2$ [130].

Defining $b_1 = \sum n_{CaO}$, $b_2 = \sum n_{Ce_2O_3}$, $a_1 = \sum n_{SiO_2} = 0.1$, $a_2 = \sum n_{Al_2O_3}$, these are the mass fractions of CaO, Ce_2O_3, SiO_2, and Al_2O_3, respectively. The mass action concentrations of each component are defined as follows: $N_1 = N_{CaO}$, $N_2 = N_{Ce_2O_3}$, $N_3 = N_{SiO_2}$, $N_4 = N_{Al_2O_3}$, $N_5 = N_{CaO\cdot Al_2O_3}$, $N_6 = N_{CaO\cdot 2Al_2O_3}$, $N_7 = N_{CaO\cdot 6Al_2O_3}$, $N_8 = N_{3CaO\cdot Al_2O_3}$, $N_9 = N_{12CaO\cdot 7Al_2O_3}$, $N_{10} = N_{CaSiO3}$, $N_{11} = N_{Ca2SiO4}$, $N_{12} = N_{Ca3SiO5}$, $N_{13} = N_{Ce_2O_3\cdot Al_2O_3}$, $N_{14} = N_{Ce_2O_3\cdot 11Al_2O_3}$, $N_{15} = N_{CaO\cdot Al2O3\cdot 2SiO_2}$, $N_{16} = N_{2CaO\cdot Al_2O_3\cdot SiO_2}$, and $N_{17} = N_{3Al2O3\cdot 2SiO_2}$.

The chemical equilibriums in the temperature range of 1773~1873 K can be defined as follows [130]:

$$(Ca^{2+} + O^{2-}) + Al_2O_3 = CaOAl_2O_3$$

$$\Delta G^{\Theta} = -18120 - 19.62T, N_5 = K_1 \cdot N_1 \cdot N_4 \tag{3}$$

$$(Ca^{2+} + O^{2-}) + 2Al_2O_3 = CaO \cdot 2Al_2O_3$$

$$\Delta G^{\Theta} = -16400 - 26.8T, N_6 = K_2 \cdot N_1 \cdot {N_4}^2 \tag{4}$$

$$\left(Ca^{2+} + O^{2-}\right) + 6Al_2O_3 = CaO \cdot 6Al_2O_3$$

$$\Delta G^{\Theta} = -17430 - 37.2T, N_7 = K_3 \cdot N_1 \cdot {N_4}^6 \tag{5}$$

$$3\left(Ca^{2+} + O^{2-}\right) + Al_2O_3 = 3CaO \cdot Al_2O_3$$

$$\Delta G^{\Theta} = -17000 - 32.0T, N_8 = K_4 \cdot {N_1}^3 \cdot N_4 \tag{6}$$

$$12\left(Ca^{2+} + O^{2-}\right) + 7Al_2O_3 = 12CaO \cdot 7Al_2O_3$$

$$\Delta G^{\Theta} = -86100 - 205.1T, N_9 = K_5 \cdot {N_1}^{12} \cdot {N_4}^7 \tag{7}$$

$$\left(Ca^{2+}+O^{2-}\right)+SiO_2=CaSiO_3$$

$$\Delta G^{\Theta}=-81416-10.498T, N_{10}=K_6\cdot N_1\cdot N_3 \tag{8}$$

$$2\left(Ca^{2+}+O^{2-}\right)+SiO_2=Ca_2SiO_4$$

$$\Delta G^{\Theta}=-160431+4.016T, N_{11}=K_7\cdot {N_1}^2\cdot N_3 \tag{9}$$

$$3\left(Ca^{2+}+O^{2-}\right)+SiO_2=Ca_3SiO_5$$

$$\Delta G^{\Theta}=93366-23.03T, N_{12}=K_8\cdot {N_1}^3\cdot N_3 \tag{10}$$

$$\left(2Ce^{3+}+3O^{2-}\right)+Al_2O_3=Ce_2O_3\cdot Al_2O_3$$

$$\Delta G^{\Theta}=-58555.5-15.04T, N_{13}=K_9\cdot N_2\cdot N_4 \tag{11}$$

$$\left(2Ce^{3+}+3O^{2-}\right)+11Al_2O_3=Ce_2O_3\cdot 11Al_2O_3$$

$$\Delta G^{\Theta}=-49323-80.56T, N_{14}=K_{10}\cdot N_2\cdot {N_4}^{11} \tag{12}$$

$$\left(Ca^{2+}+O^{2-}\right)+Al_2O_3+2SiO_2=CaO\times Al_2O_3\cdot 2SiO_2$$

$$\Delta G^{\Theta}=-13816.44-55.266T, N_{15}=K_{11}\cdot N_1\cdot N_4\cdot N_3^2 \tag{13}$$

$$2\left(Ca^{2+}+O^{2-}\right)+Al_2O_3+SiO_2=2CaO\cdot Al_2O_3\cdot SiO_2$$

$$\Delta G^{\Theta}=-61964.64-60.29T, N_{16}=K_{12}\cdot {N_1}^2\cdot N_4\cdot N_3 \tag{14}$$

$$3Al_2O_3+2SiO_2=3Al_2O_3\cdot 2SiO_2$$

$$\Delta G^{\Theta}=-4351-10.46T, N_{17}=K_{13}\cdot {N_4}^3\cdot N_3^2 \tag{15}$$

The equilibrium constants K_i of all reactions satisfy the expression $\Delta G^{\Theta} = -R\cdot T\cdot lnK_i$; K_i can be calculated using the following formula:

$$K_i=\exp\left(\frac{\Delta G^{\Theta}}{RT}\right) \tag{16}$$

where ΔG^{Θ} is the change of the reaction-free energy of each reaction.

The total equilibrium mole number of all structural units in the CaO-Ce_2O_3-SiO_2-Al_2O_3 slag system can be expressed as:

$$\begin{aligned}\sum n_i = 2n_1+5n_2+n_3+n_4+n_5+n_6+n_7+n_8+n_9+n_{10}\\ +n_{11}+n_{12}+n_{13}+n_{14}+n_{15}+n_{16}+n_{17}\end{aligned} \tag{17}$$

where, n_i corresponds to the mole number of 17 substances existing in the slag, $N_i = n_i/\sum n_i$, but for the ion-pairs ($2Ce^{3+} + 3O^{2-}$) and ($Ca^{2+} + O^{2-}$) existing in the slag, $N_{Ce_2O_3} = N_{Ce}{}^{3+} + N_O{}^{2-} = (2n_{Ce}{}^{3+} + 3n_O{}^{2-})/(\sum n_i) = 5n_{Ce_2O_3}/\sum n_i$, ($Ca^{2+} + O^{2-}$) is calculated in the same way as ($2Ce^{3+} + 3O^{2-}$).

According to mass equilibrium, the following formulas could be obtained:

$$b_1=\sum n_i\cdot\begin{pmatrix}0.5N_1+N_5+N_6+N_7+3N_9+N_{10}+2N_{11}\\ +3N_{12}+N_{15}+12N_{16}\end{pmatrix} \tag{18}$$

$$b_2=\sum n_i\cdot(0.2N_2+N_{13}+N_{14}) \tag{19}$$

$$a_1=\sum n_i\cdot(N_3+N_{10}+N_{11}+N_{12}+2N_{15}+N_{16}+2N_{17}) \tag{20}$$

$$a_2=\sum n_i\cdot\begin{pmatrix}N_4+N_5+2N_6+6N_7+N_8+7N_9+N_{13}\\ +11N_{14}+N_{15}+N_{16}+3N_{17}\end{pmatrix} \tag{21}$$

$$N_1 + N_2 + N_3 + N_4 + N_5 + N_6 + N_7 + N_8 + N_9 + N_{10} \\ +N_{11} + N_{12} + N_{13} + N_{14} + N_{15} + N_{16} + N_{17} = 1 \quad (22)$$

Therefore, Equations (3)–(15) and (18)–(22) are the governing equations of the developed thermodynamic model for calculating the mass action concentrations N_i of the structural units or ion couples in the CaO-Ce_2O_3-SiO_2-Al_2O_3 slag. Specifically, the values of N_1, N_2, N_3, and N_4 can be obtained by solving the Equation set (18)–(22), by taking Equations (3)–(15) and the specific values of T, b_1, b_2, and a_2 as the initial conditions. Then, N_5–N_{17} can be solved by substituting N_1–N_4 into Equations (3)–(15). Newton's iteration method is used in the process of solving the equation set.

The calculated results of the mass action concentration (activity) and the surface tension are identical to the calculation results of Wu et al. [130], which have been validated with experimental results. The total average deviation of the model was 4–9% [154–156].

(2) Surface tension calculation

Extending the ion and molecule coexistence theory from inside of the slag to the surface, the surface mass action concentrations are defined as follows: ${N_1}^S = N^S{}_{CaO}$, ${N_2}^S = N^S{}_{Ce_2O_3}$, ${N_3}^S = N^S{}_{SiO_2}$, ${N_4}^S = N^S{}_{Al_2O_3}$, ${N_5}^S = N^S{}_{CaO\cdot Al_2O_3}$, ${N_6}^S = N^S{}_{CaO\cdot 2Al_2O_3}$, ${N_7}^S = N^S{}_{CaO\cdot 6Al_2O_3}$, ${N_8}^S = N^S{}_{3CaO\cdot Al_2O_3}$, ${N_9}^S = N^S{}_{12CaO\cdot 7Al_2O_3}$, ${N_{10}}^S = N^S{}_{CaSiO3}$, ${N_{11}}^S = N^S{}_{Ca2SiO4}$, ${N_{12}}^S = N^S{}_{Ca3SiO5}$, ${N_{13}}^S = N^S{}_{Ce_2O_3\cdot Al_2O_3}$, ${N_{14}}^S = N^S{}_{Ce_2O_3\cdot 11Al_2O_3}$, ${N_{15}}^S = N^S{}_{CaO\cdot Al_2O_3\cdot 2SiO_2}$, ${N_{16}}^S = N^S{}_{2CaO\cdot Al_2O_3\cdot SiO_2}$, and ${N_{17}}^S = N^S{}_{3Al_2O_3\cdot 2SiO_2}$.

According to the mass conservation:

$$N_1^S + N_2^S + N_3^S + N_4^S + N_5^S + N_6^S + N_7^S + N_8^S + N_9^S + N_{10}^S \\ +N_{11}^S + N_{12}^S + N_{13}^S + N_{14}^S + N_{15}^S + N_{16}^S + N_{17}^S = 1 \quad (23)$$

A new equation containing only ${N_1}^S$, ${N_2}^S$, ${N_3}^S$, and ${N_4}^S$ is obtained by substituting the surface mass action concentration into the equilibrium constant expression in Equations (3)–(15), and then substituting the results into Equation (23).

According to the Equation (1), the Butler equation corresponding to the CaO-Ce_2O_3-SiO_2-Al_2O_3 slag system can be written in the following form:

$$\sigma_{CaO-Ce_2O_3-SiO_2-Al_2O_3} = \sigma^0_{CaO} + \frac{RT}{A_{CaO}} ln \frac{N_1^s}{N_1} \quad (24)$$

$$= \sigma^0_{Ce_2O_3} + \frac{RT}{A_{Ce_2O_3}} ln \frac{N_2^s}{N_2} \quad (25)$$

$$= \sigma^0_{SiO_2} + \frac{RT}{A_{SiO_2}} ln \frac{N_3^s}{N_3} \quad (26)$$

$$= \sigma^0_{Al_2O_3} + \frac{RT}{A_{Al_2O_3}} ln \frac{N_4^s}{N_4} \quad (27)$$

Three new equations are obtained by subtracting (25)–(27) from (24), respectively, and the equation simplified by (23) is formed into a set of equations. The values of ${N_1}^S$, ${N_2}^S$, ${N_3}^S$, and ${N_4}^S$ can be gained by solving the equations. The surface tension of the CaO-Ce_2O_3-SiO_2-Al_2O_3 slag system can be acquired by substituting the values of ${N_1}^S$, ${N_2}^S$, ${N_3}^S$, and ${N_4}^S$ into one of the Equations of (24)–(27).

To calculate the surface tension of this slag system, the surface tension and molar volume data of each component are also required, which can be found in references [109,148], and are listed in Table 5.

The surface tension and molar volume of Ce_2O_3 cannot be found in the available literatures. However, the data of rare earth lanthanide elements can be found in references [134,147], and they are listed in Table 6.

According to the data in Table 6, the relationship between the molar volume (m^3/mol) of Ce_2O_3 and temperature (K) is reasonably estimated to be 49.0 [1 + 1·10^{-4}·(T-1773)]·10^{-6},

and the surface tension of Ce_2O_3 at 1873 K is estimated to be 680 × 10^{-3} N/m. The surface tension at 1773 K is 690 × 10^{-3} N/m.

Table 5. The relationships between surface tension and molar volume of pure components and temperature.

Component	Relationship between Surface Tension (×10^{-3} N/m) and Temperature (K)	Relationship between Molar Volume (m^3/mol) and Temperature (K)
CaO	791 − 0.0935 T	20.7 [1 + 1·10^{-4}·(T-1773)]·10^{-6}
Al_2O_3	1024 − 0.177 T	28.3 [1 + 1·10^{-4}·(T-1773)]·10^{-6}
SiO_2	243.2 + 0.031 T	27.516 [1 + 1·10^{-4}·(T-1773)]·10^{-6}
MgO	1770 − 0.636 T	16.1 [1 + 1·10^{-4}·(T-1773)]·10^{-6}

Table 6. Surface tension and molar volume data for several lanthanide oxides.

Element	Oxide	Surface Tension (×10^{-3} N/m, 1873 K)	Surface Tension (×10^{-3} N/m, 2573 K)	Relationship between Molar Volume (m^3/mol) and Temperature (K)
La	La_2O_3	686 (Solid)	560 (Liquid)	50.1 [1 + 1·10^{-4}·(T-1773)]·10^{-6}
Ce	Ce_2O_3	To be estimated	Unknown	To be estimated
Nd	Nd_2O_3	677 (Solid)	Unknown	46.62 [1 + 1·10^{-4}·(T-1773)]·10^{-6}
Sm	Sm_2O_3	Unknown	815 (Liquid)	47.93 [1 + 1·10^{-4}·(T-1773)]·10^{-6}
Gd	Gd_2O_3	664 (solid)	Unknown	49.09 [1 + 1·10^{-4}·(T-1773)]·10^{-6}

After calculating via MATLAB software, the surface tension data of the CaO-Ce_2O_3-SiO_2-Al_2O_3 slag system are obtained and listed in Table 7. It should be noted that the surface tension varies within a limited range.

Table 7. Surface tension of CaO-Ce_2O_3-SiO_2-Al_2O_3 slag system at 1773 K.

Serial	CaO %wt	Al_2O_3 %wt	SiO_2 %wt	Ce_2O_3 %wt	Basicity C/A	Surface Tension (N/m)
A1	54.64	30.36	10	5	1.8	0.5693
A2	51.00	34.00	10	5	1.5	0.5690
A3	46.36	38.64	10	5	1.2	0.5693
A4	51.43	28.57	10	10	1.8	0.5682
A5	48.21	26.79	10	15	1.8	0.5670

2.1.4. Surface Tension Calculation of the CaO-Ce_2O_3-SiO_2-Al_2O_3-MgO Slag System

Compared with the CaO-Ce_2O_3-SiO_2-Al_2O_3 slag system, the CaO-Ce_2O_3-SiO_2-Al_2O_3-MgO slag system increases by one more ion Mg^{2+}, one more simple molecule MgO, and five more complex molecules MgO·Al_2O_3, MgO·SiO_2, Mg_2SiO_4, CaO·MgO·2SiO_2, and 2CaO·MgO·2SiO_2. The mass action concentration of each component was defined as follows: $N_{18} = N_{MgO}$, $N_{19} = N_{MgO\cdot Al_2O_3}$, $N_{20} = N_{MgO\cdot SiO_2}$, $N_{21} = N_{Mg2SiO4}$, $N_{22} = N_{CaO\cdot MgO\cdot 2SiO_2}$, and $N_{23} = N_{2CaO\cdot MgO\cdot 2SiO_2}$. The following five equilibrium reactions are required:

$$\left(Mg^{2+}+O^{2-}\right)+Al_2O_3= MgO\cdot Al_2O_3$$

$$\Delta G^{\Theta} = -35530 - 17.39T, N_{19} = K_{14}\cdot N_{18}\cdot N_4 \quad (28)$$

$$\left(Mg^{2+}+O^{2-}\right)+SiO_2= MgO\cdot SiO_2$$

$$\Delta G^{\Theta} = -41089.4 - 6.10T, N_{20} = K_{15}\cdot N_{18}\cdot N_3 \quad (29)$$

$$2\left(Mg^{2+}+O^{2-}\right)+SiO_2= 2MgO\cdot SiO_2$$

$$\Delta G^{\Theta} = -67130.8 - 2.508T, N_{21} = K_{16}\cdot N_{18}^2\cdot N_3 \quad (30)$$

$$\left(Ca^{2+}+O^{2-}\right)+\left(Mg^{2+}+O^{2-}\right)+2SiO_2=CaO\cdot MgO\cdot 2SiO_2$$
$$\Delta G^{\Theta}=-162602+18.81T, N_{22}=K_{17}\cdot N_1\cdot N_{18}\cdot N_3^2 \quad (31)$$
$$2\left(Ca^{2+}+O^{2-}\right)+\left(Mg^{2+}+O^{2-}\right)+2SiO_2=2CaO\cdot MgO\cdot 2SiO_2$$
$$\Delta G^{\Theta}=-73688-63.639T, N_{23}=N_1^2\cdot N_{18}\cdot N_3^2 \quad (32)$$

The surface tension of the CaO-Ce_2O_3-SiO_2-Al_2O_3-MgO slag system is calculated by using the existing data and calculation methods described in Section 2.1.3. The results are shown in Table 8.

Table 8. Surface tension of CaO-Ce_2O_3-SiO_2-Al_2O_3-MgO slag system at 1823 K.

Serial	CaO %wt	Al_2O_3 %wt	SiO_2 %wt	MgO %wt	Ce_2O_3 %wt	Surface Tension (N/m)
C0	48	37.5	4.5	10	0	0.5992
C1	45	37.5	4.5	10	3	0.6725
C2	46.2	36.3	4.5	10	3	0.6735
C3	45	35.5	4.5	10	5	0.6736
C4	43.4	34.1	4.5	10	8	0.6740
C5	45	32.5	4.5	10	8	0.6754

2.2. Calculation Model of Interfacial Tension

According to Girifalco-Good equation, the interfacial tension between inclusions and molten steel, between inclusions and slag, and between slag and steel are calculated.

Girifalco-Good equation [157]:

$$\sigma_{ab}=\sigma_a+\sigma_b-2\varphi_{ab}\sqrt{\sigma_a\cdot\sigma_b} \quad (33)$$

where the subscripts a and b represent the two phases, σ_{ab} is the interfacial tension between phases a and b, σ_a and σ_b are the surface tensions of each phase, and φ_{ab} represents the interaction coefficient between a and b.

2.2.1. Interfacial Tension between Inclusion and Molten Steel

This section mainly refers to the research results of Nakajima [158]. According to the Girifalco-Good equation, the interfacial tension between inclusions and molten steel can be expressed as:

$$\sigma_{IM}=\sigma_I+\sigma_M-2\cdot\varphi_{IM}\sqrt{\sigma_I\cdot\sigma_M} \quad (34)$$

The surface tension σ_I of Al_2O_3 inclusions is 0.75 N/m. To calculate the surface tension σ_M of molten steel, as a simplification, only a certain content of O and S are considered in steel. Then, the surface tension of liquid steel is expressed as follows:

$$\sigma_M=\begin{bmatrix}1910-825\cdot log_{10}(1+210\cdot[O])\\-540\cdot log_{10}(1+185\cdot[S])\end{bmatrix}\cdot 10^{-3}(\mathrm{N/m})$$
$$([S]\leq 0.18wt\%, [O]\leq 0.015wt\%) \quad (35)$$

In this study, [S] = 0.005%, [O] = 0.0025%, and σ_M = 1.6052 N/m.

The interaction coefficient between solid inclusions and molten steel:

$$\varphi_{IM}=0.351-0.507\cdot(R-1) \quad (36)$$

where R is the surface roughness of the inclusion, and its value ranges over 1.0~1.36.

Ideally, the surface roughness of the inclusion is 1, so that φ_{IM} = 0.351. Substituting all the data into Equation (35), we can obtain σ_{IM} = 1.585 N/m.

2.2.2. Interfacial Tension between Inclusion and Slag

The interfacial tension between inclusion and slag can be expressed as follows:

$$\sigma_{IS} = \sigma_I + \sigma_S - 2 \cdot \varphi_{IS}\sqrt{\sigma_I \cdot \sigma_S} \tag{37}$$

The surface tension between the inclusion and slag has been obtained. The interaction coefficient φ_{IS} between the inclusion and slag is required.

The interaction coefficient between the Al_2O_3 inclusion and the CaO-SiO_2-Al_2O_3-MgO-CaF_2-Na_2O slag system was studied in reference [158]; φ_{IS} is expressed as:

$$\begin{aligned}\varphi_{IS} &= 0.947 \times X_{Al_2O_3} + 0 \times X_{SiO_2} + 0.602 \times X_{CaF_2} + 0.601 \times X_{MgO} \\ &+0.545 \times X_{CaO} + 0.475 \times X_{Na_2O} + 0.705 \times X_{Al_2O_3} \times X_{CaO} \\ &-0.609 \times X_{Al_2O_3} \times X_{SiO_2} + 1.564 \times X_{SiO_2} \times X_{CaO} \\ &+0 \times X_{CaF_2} \times X_{CaO} + 0.755 \times X_{CaF_2} \times X_{SiO_2} \\ &+1.292 \times X_{SiO_2} \times X_{MgO} + 1.156 \times X_{SiO_2} \times X_{Na_2O}\end{aligned} \tag{38}$$

where X_{CaO}, X_{SiO_2}, $X_{Al_2O_3}$, X_{MgO}, X_{CaF2}, and X_{Na2O} are the molar fractions of each component.

The interaction coefficient between the slag system and the Al_2O_3 inclusion was studied in the research results of Nakajima [158], as shown in Table 9.

Table 9. Measured data of interaction coefficient between slag system and Al_2O_3 inclusion.

X_{CaO}	$X_{Al_2O_3}$	X_{SiO_2}	X_{MgO}	φ_{IS}
0.453	0.125	0.423	0	0.630
0.486	0.059	0.454	0	0.701
0.342	0.125	0.532	0	0.564
0.673	0.287	0.035	0.005	0.820
0.673	0.287	0.035	0.005	0.821

According to the data in the literature and theoretical analysis, φ_{IS} = 0.8 is estimated for the CaO-Ce_2O_3-SiO_2-Al_2O_3 slag system.

For the CaO-Ce_2O_3-SiO_2-Al_2O_3-MgO slag system, the interaction coefficient is calculated by Equation (38), ignoring the effect of Ce_2O_3. The calculation results are shown in Table 10.

Table 10. Interaction coefficient between inclusion and slag (ignoring the effect of $X_{Ce_2O_3}$).

Serial	X_{CaO}	$X_{Al_2O_3}$	X_{SiO_2}	X_{MgO}	$X_{Ce_2O_3}$	φ_{IS}
C0	0.5531	0.2371	0.0484	0.1613	0	0.7603
C1	0.5338	0.2442	0.0498	0.1661	0.0061	0.7588
C2	0.5445	0.2349	0.0495	0.165	0.006	0.7542
C3	0.5386	0.2333	0.0503	0.1676	0.0102	0.7499
C4	0.5313	0.2292	0.0514	0.1714	0.0167	0.7424
C5	0.5461	0.2165	0.051	0.1699	0.0166	0.7361

Based on the calculated data, considering the stronger interaction between slag containing Ce_2O_3 and Al_2O_3, φ_{IS} = 0.75 is used for the inclusion–slag interfacial tension of slag C0, and φ_{IS} = 0.78 is used for the inclusion–slag interfacial tension of slag C1–C5.

By substituting σ_I, σ_S, and φ_{IS} of slags with different compositions into Equation (37), σ_{IS} is calculated.

2.2.3. Interfacial Tension between Slag and Steel

The interfacial tension between slag and steel can be expressed as:

$$\sigma_{MS} = \sigma_M + \sigma_S - 2 \cdot \varphi_{MS}\sqrt{\sigma_M \cdot \sigma_S} \tag{39}$$

For the CaO-SiO_2-Al_2O_3-MgO-CaF_2-Na_2O slag system studied in reference [158], the interaction coefficient between slag and steel is expressed as:

$$\begin{aligned}\varphi_{MS} &= 0.576 \times X_{SiO_2} + 0.399 \times X_{Al_2O_3} + 0.326 \times X_{CaF_2} + 0.687 \times X_{MgO} \\ &+0.607 \times X_{CaO} - 0.675 \times X_{SiO_2} \times X_{CaO} + 0.338 \times X_{SiO_2} \times X_{Al_2O_3} \\ &-0.391 \times X_{Al_2O_3} \times X_{CaO} - 0.892 \times X_{Al_2O_3} \times X_{CaF_2} \\ &-1.701 \times X_{MgO} \times X_{SiO_2} - 0.27 \times X_{MgO} \times X_{Al_2O_3}\end{aligned} \tag{40}$$

The relevant data of Ce_2O_3 cannot be found in the literature, so that the interaction coefficient between the CaO-Ce_2O_3-SiO_2-Al_2O_3 slag system and molten steel needs to be reasonably estimated. The CaO-SiO_2-Al_2O_3-MgO slag system is referred, and the interaction coefficient between slag and steel in reference [158] is listed in Table 11.

Table 11. Measured data of interaction coefficient between CaO-SiO_2-Al_2O_3-MgO slag system and steel.

X_{CaO}	$X_{Al_2O_3}$	X_{SiO_2}	X_{MgO}	φ_{MS}
0.536	0.246	0.168	0.050	0.439
0.604	0.277	0.068	0.051	0.433
0.481	0.287	0.165	0.067	0.432
0.514	0.306	0.109	0.072	0.453
0.544	0.324	0.056	0.076	0.454
0.505	0.233	0.164	0.098	0.438
0.572	0.262	0.067	0.099	0.428
0.466	0.215	0.160	0.159	0.435
0.531	0.243	0.065	0.161	0.429

It is observed that the interaction coefficient between the CaO-Al_2O_3-SiO_2-MgO slag system, which is similar to the CaO-Ce_2O_3-SiO_2-Al_2O_3 slag system studied in this paper, and steel, ranges from 0.428 to 0.454. The average value of the interaction coefficient between CaO-Ce_2O_3-SiO_2-Al_2O_3 slag and liquid steel is about 0.43. In order to improve the accuracy of the interaction coefficient, it is modified according to the following analysis.

In Section 2.3, the motion model of inclusion at the slag–steel interface, the overall wettability $cos\theta_{IMS}$ of the steel–slag inclusion system is required:

$$cos\theta_{IMS} = \frac{\sigma_{IM} - \sigma_{IS}}{\sigma_{MS}} \tag{41}$$

The relationship between σ_{IM}, σ_{IS}, σ_{MS}, and θ_{IMS} is shown in Figure 2. There are two wetting states between slag and inclusion, as shown in Figure 2a; $cos\theta_{IMS} > 0$, which means the inclusion shows a good wettability for slag. If $cos\theta_{IMS} < 0$, as shown in Figure 2b, this means that the inclusion shows a poor wettability for slag.

It can be seen that $cos\theta_{IMS}$ increases with the decrease in σ_{IS} or σ_{MS}, so that the slag–steel interaction coefficient should be reduced to a smaller value to compensate for the deficiency where σ_{IS} may be too large, which is beneficial for improving the accuracy of the calculation model. Therefore, for CaO-Ce_2O_3-SiO_2-Al_2O_3 slag system, φ_{MS} = 0.4 is used in the calculation.

By substituting σ_M, σ_S, and φ_{MS} into Equation (39), the interfacial tension σ_{MS} between the CaO-Ce_2O_3-SiO_2-Al_2O_3 slag system and molten steel can be obtained.

For the CaO-Ce_2O_3-SiO_2-Al_2O_3-MgO slag system, the slag composition is close to the slags in Table 11. Thus, the interaction coefficient between slag and steel is referred to in Table 11. Therefore, φ_{MS} = 0.43 is used in the calculation of the steel–slag interfacial tension of slag C0 without Ce_2O_3. Considering that the interaction between slag containing Ce_2O_3 and molten steel will be strengthened, φ_{MS} = 0.45 is estimated in the calculation of slag C1–C5. In the same way, the interfacial tension σ_{MS} between the CaO-Ce_2O_3-SiO_2-Al_2O_3-MgO slag system and molten steel can be obtained.

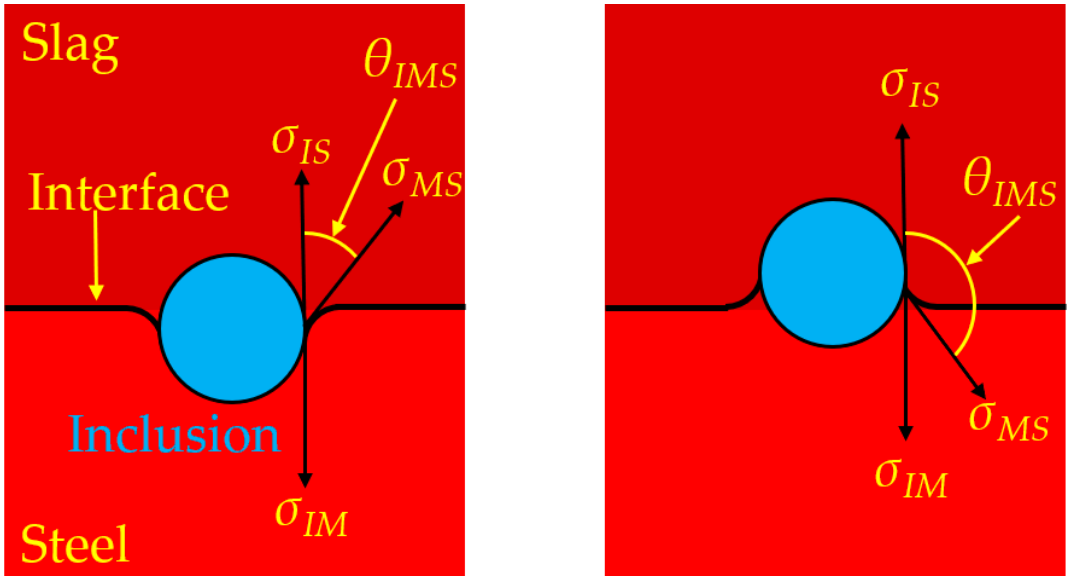

(**a**) (**b**)

Figure 2. The relationship between σ_{IM}, σ_{IS}, σ_{MS}, and θ_{IMS}. (**a**) $cos\theta_{IMS} > 0$, (**b**) $cos\theta_{IMS} < 0$.

2.2.4. Interfacial Tension Summary

All of the calculation results of the two slag systems are summarized in Tables 12 and 13.

Table 12. Interfacial properties of the CaO-Ce_2O_3-SiO_2-Al_2O_3 slag system at 1773 K.

Serial	σ_{IM} (N/m)	σ_{IS} (N/m)	σ_{MS} (N/m)	Overall Wettability $cos\theta_{IMS}$
A1	1.585	0.2738	1.4097	0.9301
A2		0.2738	1.4096	0.9302
A3		0.2738	1.4097	0.9301
A4		0.2737	1.4094	0.9304
A5		0.2736	1.4090	0.9307

Table 13. Interfacial properties of the CaO-Ce_2O_3-SiO_2-Al_2O_3-MgO slag system at 1823 K.

Serial	σ_{IM} (N/m)	σ_{IS} (N/m)	σ_{MS} (N/m)	Overall Wettability $cos\theta_{IMS}$
C0	1.585	0.3436	1.3610	0.9121
C1		0.3146	1.3426	0.9462
C2		0.3148	1.3429	0.9459
C3		0.3148	1.3430	0.9458
C4		0.3149	1.3431	0.9457
C5		0.3151	1.3435	0.9452

2.3. Motion Model of Inclusion at the Steel–Slag Interface

The interfacial tension data calculated in the above sections will be used in the motion model of inclusions that will be described in this section.

2.3.1. Assumptions of This Model

The basic assumptions of this mathematical motion model of inclusions at the steel–slag interface are listed as follows:

(1) The inclusions are spherical in constant volume;
(2) No chemical reaction occurs between the phase interfaces;
(3) All fluids are incompressible and isothermal;
(4) The slag phase exists in liquid form;

(5) The steel–slag interface is smooth;

(6) The movement process of inclusions depends on the force balance between the buoyancy force, rebound force, drag force, and the fluid added mass force;

(7) The surface tension is uniform at the interface.

As proposed by Nakajima and Okamura [71], when the inclusion approaches the slag–steel interface, a steel film forms when Re $\geq$ 1, otherwise, the inclusion contacts with the slag directly without steel film formation. The Reynolds number of inclusions is defined as:

$$Re = \frac{2\rho_M u_\infty R_I}{\mu_M} \tag{42}$$

where R_I is the radius of inclusion, ρ_M is the density of molten steel, μ_M is the viscosity of the molten steel, and u_∞ is the velocity of inclusion.

In the studied small size of the inclusion cases, for example, if the diameter is less than 150 μm, the Reynolds number is less than 1. Thus, the model of non-steel film could be used. In this paper, the motion behavior of the inclusion is studied at the steel–slag interface. Specifically, the inclusion is at an initial position below the slag; that is, when t = 0, the displacement from the center of inclusion to the interface Z = 0, as shown in Figure 3. Then, there are three kinds of interfacial motion behaviors of the inclusions: Pass (P), Oscillate (O), and Remain (R). "Pass" means that the displacement of the inclusion is higher than two times the radius, the motion path of inclusions is 1→2→3, as shown in Figure 3a. "Oscillate" means that the inclusions oscillate but do not penetrate the slag–steel interface, and the motion path of the inclusions is 1→2→3→4, as shown in Figure 3c. "Remain" means that the displacement of inclusion is less than two times the radius, and the motion path of the inclusions is 1→2→3, as shown in Figure 3b. When it moves up by two times their radius $2R_I$, as shown in Figure 3a, it is considered to be completely separated from the molten steel into the slag.

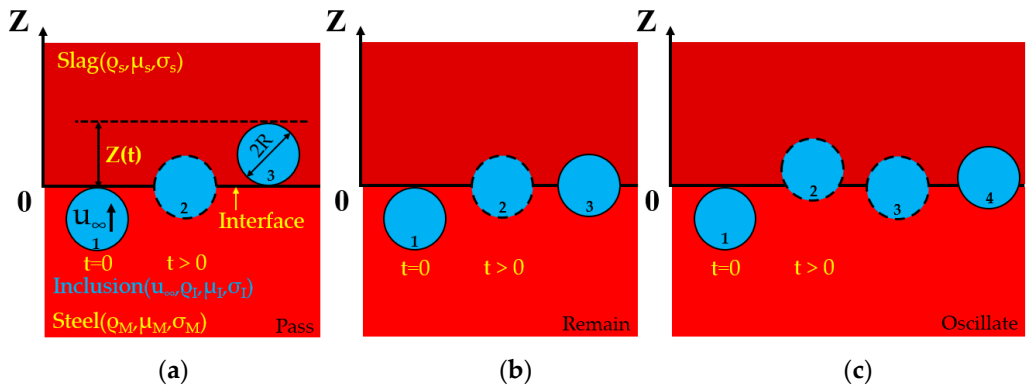

Figure 3. Three kinds of interfacial motion behaviors of inclusions (**a**) Pass, (**b**) Remain, (**c**) Oscillate.

The initial floating velocity of inclusions is expressed by the Stokes velocity, and the Stokes velocity of liquid inclusions (such as 50%wtAl_2O_3–50%wtCaO) can be expressed as:

$$u_\infty = \frac{2}{3} R_I^2 (\rho_M - \rho_I) \frac{g}{\mu_M} \frac{(1+\kappa)}{(2+3\kappa)} \tag{43}$$

where ρ_I is the density of inclusions; g is the acceleration of gravity; $\kappa = \mu_I/\mu_M$, μ_I is the viscosity of inclusion, and μ_M is the viscosity of molten steel.

In this study, ρ_M = 7000 kg/m^3, μ_M = 0.006 Pa·s. ρ_I = 2814 kg/m^3, μ_I = 0.118 Pa·s, and $\kappa = \mu_I/\mu_M$ =19.67 for liquid inclusion 50%wtAl_2O_3–50%wtCaO.

For solid inclusions (such as Al_2O_3), $\kappa \to \infty$, ρ_I = 3990 kg/m^3, the Stokes velocity of this inclusion can be expressed as:

$$u_\infty = \frac{2}{9} R_I^2 (\rho_M - \rho_I) \frac{g}{\mu_M} \tag{44}$$

2.3.2. Motion Equation of Inclusion

When the inclusions move across the slag–steel interface, four forces act on the inclusions, i.e., the buoyancy force F_b, rebound force F_r, drag force F_d, and fluid added mass force F_f.

The buoyancy force is in an upward direction, while the rebound force, fluid added mass force, and drag force are either upward or downward, depending on the behavior of the inclusions at the interface.

According to Newton's second law:

$$\frac{4}{3}\pi R_I^3 \rho_I \frac{d^2 Z}{dt^2} = F_b - F_d - F_r - F_f \tag{45}$$

where Z is the displacement of the inclusion and t is the movement time of the inclusion.

The rebound force is defined as:

$$F_r = 2\pi R_I \sigma_{MS} H(Z^*) \tag{46}$$

where Z^* is the dimensionless displacement of the inclusion and H is a function of Z^*.

$$H(Z^*) = Z^* - 1 - \cos\theta_{IMS} \tag{47}$$

The buoyancy force is defined as:

$$F_b = \frac{4}{3}\pi R_I^3 g(\rho_S \cdot J(Z^*) - \rho_I) \tag{48}$$

where $J(Z^*)$ is the density-varying term, which describes the degree of the inclusion's entering into the slag.

$$J(Z^*) = \frac{1}{4}\left(\frac{\rho_M}{\rho_S} - 1\right) Z^{*3} - \frac{3}{4}\left(\frac{\rho_M}{\rho_S} - 1\right) Z^{*2} + \frac{\rho_M}{\rho_S} \tag{49}$$

The drag force is defined as:

$$F_d = 4\pi\sqrt{gR_I^3}\mu_S A \cdot I(Z^*)\frac{dZ^*}{dt^*} \tag{50}$$

where t^* is the dimensionless movement time of the inclusion, A is a function of κ, which is related to the viscosity of inclusions and molten steel; $I(Z^*)$ is the viscosity-varying term, which is related to the position of the inclusion relative to the interface.

$$A = \frac{2 + 3\kappa}{2(1 + \kappa)} \tag{51}$$

$$I(Z^*) = \left(\frac{\mu_M}{\mu_S} - 1\right) Z^{*2} - 2\left(\frac{\mu_M}{\mu_S} - 1\right) Z^* + \frac{\mu_M}{\mu_S} \tag{52}$$

The fluid added mass force is defined as:

$$F_f = \frac{2}{3}\pi R_I^3 g \rho_S J(Z^*)\frac{d^2 Z^*}{dt^{*2}} \tag{53}$$

Substituting Equations (46), (48), (50) and (53) into (45), the dimensionless motion equation of inclusion can be written as follows:

$$\frac{d^2 Z^*}{dt^{*2}} = \frac{2(\rho_S J(Z^*) - \rho_I)}{(\rho_S J(Z^*) + 2\rho_I)} - 3 * D(Z^*) * H(Z^*) - \frac{6A}{E(Z^*)} I(Z^*) * \frac{dZ^*}{dt^*} \tag{54}$$

where both D and E are functions of Z^*.

$$D(Z^*) = \frac{\sigma_{MS}}{gR_I^2(\rho_S J(Z^*) + 2\rho_I)} \tag{55}$$

$$E(Z^*) = \frac{\sqrt{gR_I^3}(\rho_S J(Z^*) + 2\rho_I)}{\mu_S} \tag{56}$$

The dimensionless form of displacement, time, velocity, and acceleration are defined as:

$$Z^* = \frac{Z}{R_I} \tag{57}$$

$$t^* = t\sqrt{\frac{g}{R_I}} \tag{58}$$

$$\frac{dZ^*}{dt^*} = \frac{1}{\sqrt{gR_I}}\frac{dZ}{dt} \tag{59}$$

$$\frac{d^2Z^*}{dt^{*2}} = \frac{1}{g}\frac{d^2Z}{dt^2} \tag{60}$$

The densities of slag ρ_s are 2700 kg/m^3 and 2750 kg/m^3 for the CaO-Ce_2O_3-SiO_2-Al_2O_3 slag system and the CaO-Ce_2O_3-SiO_2-Al_2O_3-MgO slag system, respectively.

By solving Equation (54), the displacement, velocity, and acceleration changes of the inclusions with time can be solved, and the force changes of the inclusions can be calculated by using the values of these parameters.

The methods for solving the force balance and the motion equation of inclusions are as follows: the Equations (54) and (46), (48), (50) and (53) are the governing equations of the developed mathematical model for calculating the dimensionless displacement $Z^*(t)$ and the force on inclusions. Specifically, by initializing the inclusion size, the governing Equation (54) of $Z^*(t)$ is solved using the ode45 function (Runge kutta algorithm) in MATLAB software with input of the calculated physical properties, as mentioned in previous sections. After the dimensionless displacement is obtained, the force can be calculated using Equations (46), (48), (50) and (53) with specific sizes of inclusions. This model is originally validated using experimental data by Nakajima and Okamura [71]. Their modeling work on inclusions movement in slags were reproduced, and the results are in good agreement with the original paper [71]. This ensures the reliability of the present simulation.

2.3.3. Model Validation

Based on the similarity theory, a water model experiment was established to verify the mathematical model. A schematic diagram of the experimental equipment is shown in Figure 4. In the experiment, silicon oil was used to simulate slag, water was used to simulate molten steel, and hollow alumina balls with 2.1 mm diameter were used to simulate inclusions. A cylindrical container with a particle release port at the bottom was filled with water, and the height of the water was 40 cm. In order to eliminate the refraction generated by the cylindrical camber, a square container was added around the cylindrical container, and the water level was higher than 40 cm. The water was covered by silicon oil with a thickness of more than 5 mm. Hollow alumina balls were released from the bottom release port stationary. A high-speed camera (FuHuang AgileDevice Revealer 5KF20S) was used to record the frame of the alumina balls touching the water–oil interface until the motion stopped.

The dimensionless displacement curve of the alumina ball moving at the water–oil interface could be obtained by processing the video shot using the high-speed camera. Meanwhile, the initial conditions of the water model in Table 14 were substituted into the mathematical model for calculation [159]. The comparison between the calculated results and the experimental results is shown in Figure 5. It can be seen from the figure that the

overall trend of the calculated value is consistent with the experimental value. After the particle reaches the water–oil interface, it floats up for a certain distance and is bounced back. The final dimensionless displacements for the experiment and model are 0.594 and 0.655, respectively. It is in good agreement, which verifies the feasibility and accuracy of the model.

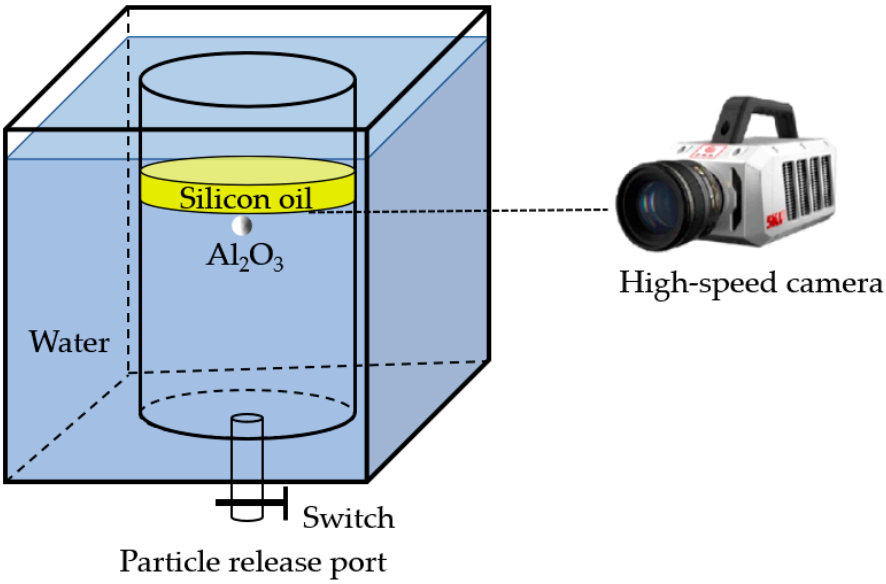

Figure 4. Schematic diagram of experimental equipment.

Table 14. Water model parameters required in calculation.

Substance	Density ($kg \cdot m^{-3}$)	Viscosity ($Pa \cdot s$)	Interfacial Tension ($N \cdot m$)			$cos\theta_{IMS}$
			Water-Oil σ_{MS}	Al_2O_3-Water σ_{IM}	Al_2O_3-Oil σ_{IS}	
Water	997	0.001				
Silicon oil	963	0.096	0.055	0.614	0.635	−0.382
Al_2O_3	710	-				

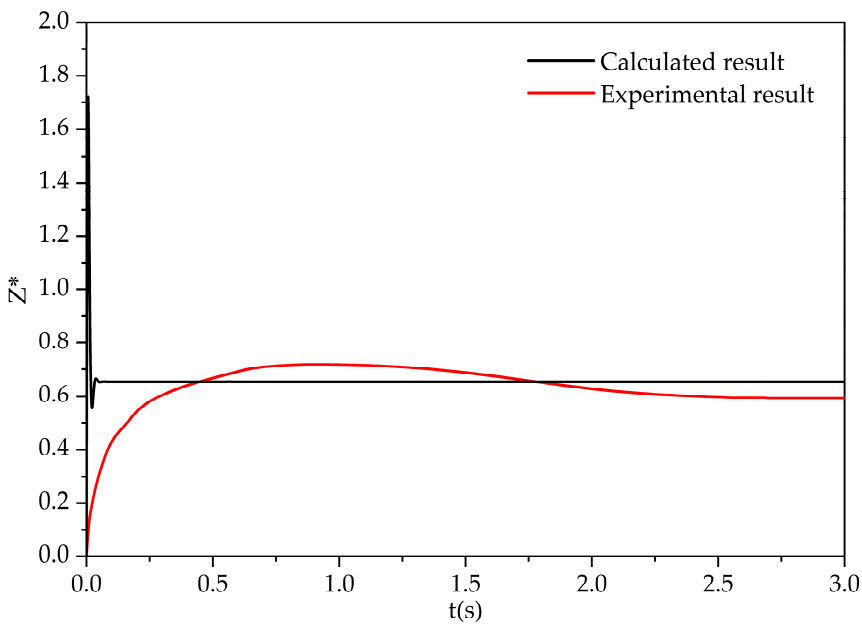

Figure 5. Comparison of experimental result and calculated result.

3. Results and Discussion

In this section, the motion behavior of solid Al_2O_3 inclusions and liquid inclusions in two slag systems are presented. The evolution of force on inclusions, and the displacement of inclusions as a function of movement time are studied. By identifying the displacement of inclusion, the motion behavior of the inclusions can be categorized as Remain, Oscillate, and Pass. Using a large number of studied cases, the force and displacement results of two typical slag systems, A5 and C3, with respect to different sizes of inclusions, are given as examples. Finally, the inclusion removal abilities of the two slag systems are compared.

3.1. Motion Behavior of Solid Al_2O_3 Inclusions in the CaO-Ce_2O_3-SiO_2-Al_2O_3 Slag System

The force of the solid Al_2O_3 inclusions with different sizes in molten steel are shown in Figure 6. The maximum value of the t axis is the time taken for the inclusions to reach force equilibrium. The force equilibrium for the inclusions is a function of moving time with different sizes. As can be seen from the figure, with the increase in the inclusion size, the time for inclusions to reach the force equilibrium in the process of motion is increasing. For all of the inclusions, the rebound force and drag force play a major role during the movement of the inclusion. With the increase in the size of inclusion, the rebound force, drag force, and fluid added mass force are increased.

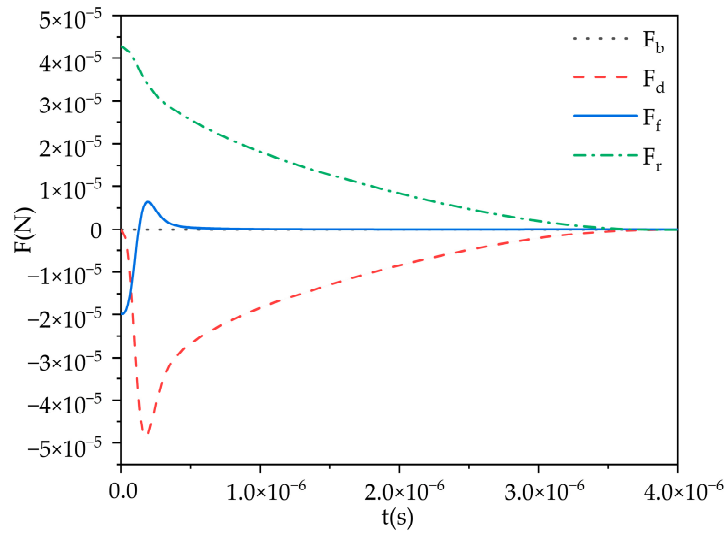

(**a**)

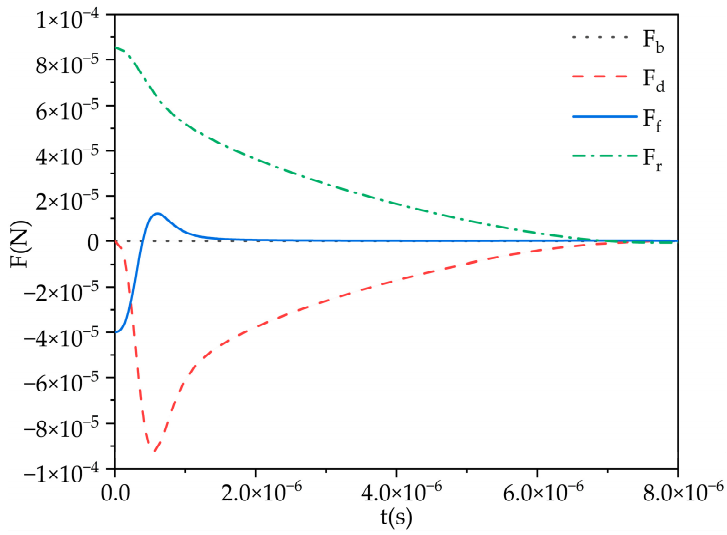

(**b**)

Figure 6. *Cont.*

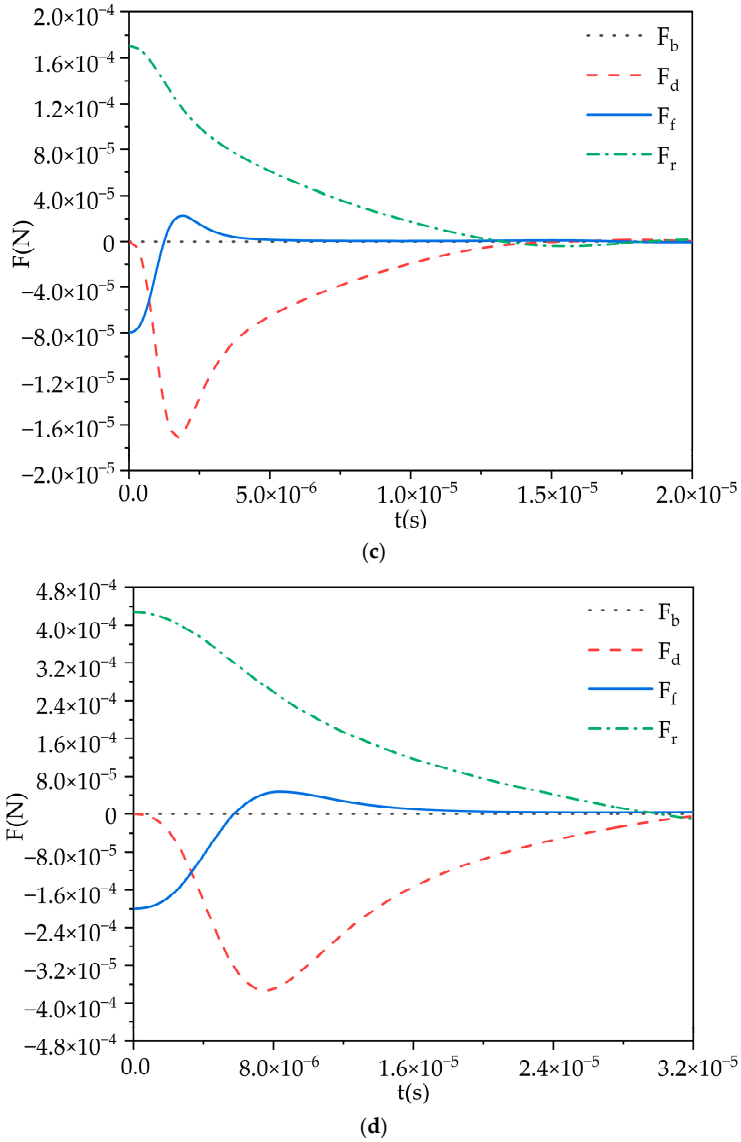

Figure 6. Force analysis of solid Al_2O_3 inclusions with different sizes, (**a**) 5 μm, (**b**) 10 μm, (**c**) 20 μm, (**d**) 50 μm.

The displacements of solid Al_2O_3 inclusions with different sizes at the steel–slag interface in slag A5 are shown in Figure 7.

According to the dimensionless displacement shown in Figure 7 and the classifications of Pass, Oscillate, and Remain, the inclusions with radiuses of 50 μm, 80 μm, and 140 μm can be categorized as the "Pass" group, and the time of inclusions passing through the slag–steel interface is prolonged with the increase in inclusion size. The inclusions with a radius of 10 μm and 20 μm can be categorized as the "Oscillate" group, and the inclusion with a radius of 5 μm can be categorized as the "Remain" group.

The motion behaviors of inclusions with different sizes in slags A1–A5 were calculated, and the results are shown in Table 15.

From Table 15, the smaller the size of the inclusion is, the more difficult it is to remove. The inclusions with a radius that is smaller than 20 μm cannot be removed in all the A series slag systems, and the inclusions with a radius of larger than 50 μm can be removed perfectly. The inclusion removal abilities of the five slags are ranked as A5 > A2 > A3 > A1 > A4. It should be noted that the viscosity of A5 is the smallest among the slags A1 to A5, indicating that the reduction in viscosity is more conducive to improving the inclusion removal abilities of the slags.

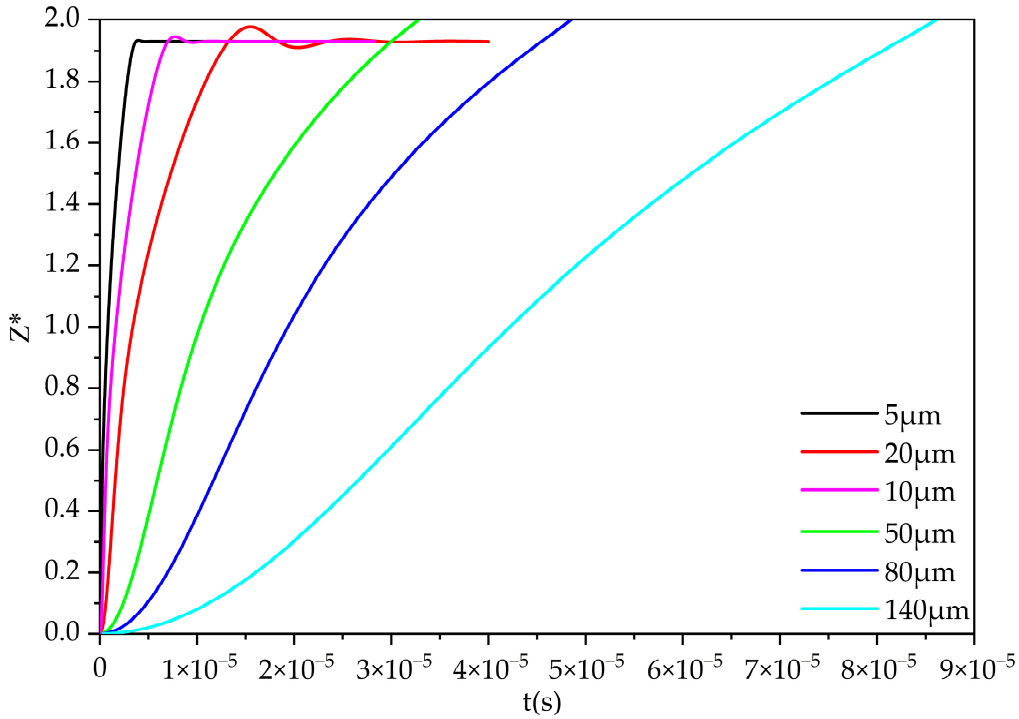

Figure 7. The displacements of solid Al_2O_3 inclusions with different radiuses of inclusions in slag A5.

Table 15. Motion behaviors of solid Al_2O_3 inclusions with different radiuses in slags A1–A5.

Radius	Slags with Different Compositions				
	A4	**A1**	**A3**	**A2**	**A5**
	51%CaO 29%Al_2O_3 10%SiO_2 10%Ce_2O_3	**55%CaO 30%Al_2O_3 10%SiO_2 5%Ce_2O_3**	**46%CaO 39%Al_2O_3 10%SiO_2 5%Ce_2O_3**	**51%CaO 34%Al_2O_3 10%SiO_2 5%Ce_2O_3**	**48%CaO 27%Al_2O_3 10%SiO_2 15%Ce_2O_3**
5 μm	R	R	R	R	R
10 μm	R	R	R	R	O
20 μm	R	O	O	O	O
50 μm	O	O	O	P	P
80 μm	P	P	P	P	P
140 μm	P	P	P	P	P

Note: R = Remain, O = Oscillate, and P = Pass.

3.2. Motion Behaviors of Liquid 50%wtAl_2O_3–50%wtCaO Inclusions in the CaO-Ce_2O_3-SiO_2-Al_2O_3 Slag System

The force of liquid 50%wtAl_2O_3-50%wtCaO inclusion in molten steel is basically similar to that of solid Al_2O_3, and it is not shown here. The displacements of the liquid 50%wtAl_2O_3–50%wtCaO inclusion at the steel–slag interface with different sizes in slag A5 are shown in Figure 8. The motion behaviors of liquid 50%wtAl_2O_3–50%wtCaO inclusions are similar to those of solid Al_2O_3 inclusions. Specifically, the inclusions with radiuses of 5 μm and 10 μm show Remain behaviors at the steel–slag interface. The 20 μm-radius inclusion exhibits oscillatory behavior. The inclusions with radiuses of 50 μm, 80 μm, and 130 μm can pass the interface and can be removed, but the time for liquid inclusions passing through the slag–steel interface is longer than for solid inclusions under the same slag condition.

The motion behaviors of liquid 50%wtAl_2O_3–50%wtCaO inclusions with different sizes in slags A1–A5 were calculated, and the results are shown in Table 16.

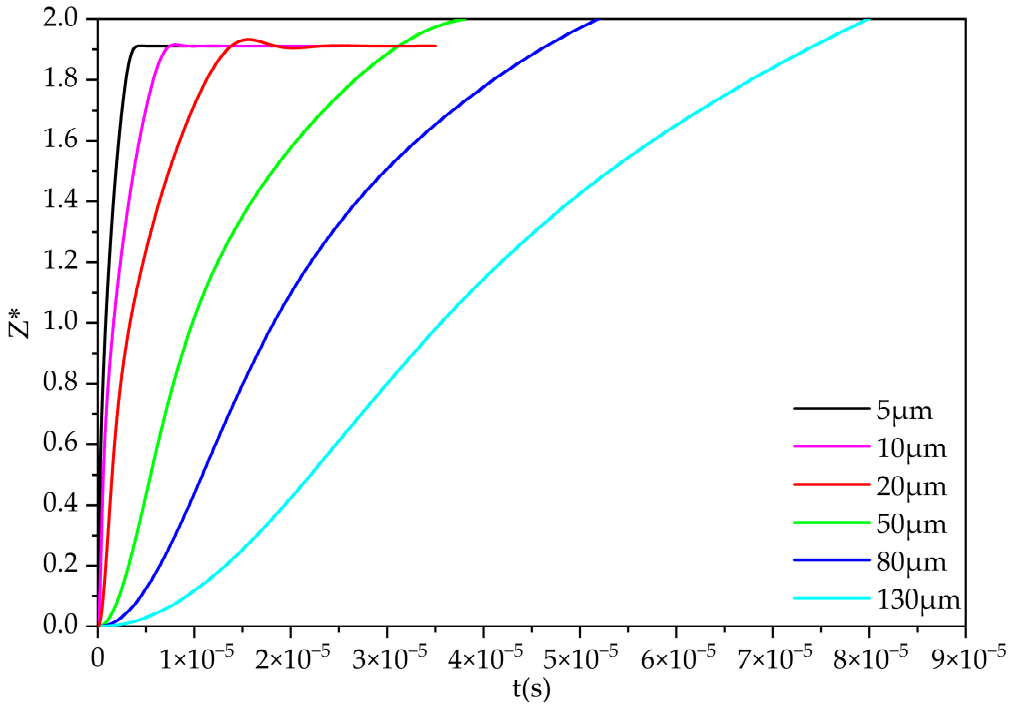

Figure 8. The displacements of liquid 50%wtAl_2O_3–50%wtCaO inclusions with different radiuses of inclusions in slag A5.

Table 16. Motion behaviors of liquid 50%wtAl_2O_3–50%wtCaO inclusions with different radiuses in slags A1–A5.

Radius	Slags of Different Compositions				
	A4	**A1**	**A3**	**A2**	**A5**
	51%CaO 29%Al_2O_3 10%SiO_2 10%Ce_2O_3	**55%CaO 30%Al_2O_3 10%SiO_2 5%Ce_2O_3**	**46%CaO 39%Al_2O_3 10%SiO_2 5%Ce_2O_3**	**51%CaO 34%Al_2O_3 10%SiO_2 5%Ce_2O_3**	**48%CaO 27%Al_2O_3 10%SiO_2 15%Ce_2O_3**
5 μm	R	R	R	R	R
10 μm	R	R	R	R	R
20 μm	R	R	R	R	O
40 μm	R	O	O	O	O
50 μm	O	O	O	O	O
80 μm	O	O	O	P	P
130 μm	O	P	P	P	P

Note: R = Remain, O = Oscillate, and P = Pass.

For liquid inclusions, the removal abilities in slags A1 to A5 are not as good as those of solid inclusions. The inclusions with a radius smaller than 50 μm are difficult to remove, and the inclusions with a radius larger than 80 μm can be removed in some of the slags. Similar to the results of solid inclusions, the inclusion removal abilities of the five slags are ranked as A5 > A2 > A3 > A1 > A4; the lower the viscosity of the refining slag is, the better the removal of inclusions.

Compared with Tables 15 and 16, from the perspective of the separation behavior of inclusions at the steel–slag interface, the solid Al_2O_3 inclusion with a radius of 20 μm showed Remain behavior in slag A4, whose viscosity is the highest of the five slags, and it showed Oscillate behavior in other slags. For the liquid inclusion with the same radius of 20 μm, it showed Oscillate behavior merely in slag A5, which posed the lowest viscosity among the five slags. In addition, the solid Al_2O_3 inclusion with a radius of 80 μm can pass the interface of all five slags, while the liquid inclusion with the same radius can only pass the interfaces of slags A2 and A5. Obviously, the size range in which the solid

inclusions can pass the interface is larger than that of liquid inclusions. Compared with Figures 7 and 8, it is easy to find that the removal time of liquid inclusions is longer than that of solid inclusions. All of these are indicating that liquid 50%wtAl_2O_3–50%wtCaO inclusions are more difficult to remove than solid Al_2O_3 inclusions.

3.3. Motion Behaviors of Solid Al_2O_3 Inclusions in the CaO-Ce_2O_3-SiO_2-Al_2O_3-MgO Slag System

The displacement of solid Al_2O_3 inclusions with different sizes at the steel–slag interface in slag C3 is shown in Figure 9. As can be seen from Figure 9, the inclusions with a radius of 20 μm, 50 μm, 80 μm, and 140 μm can be removed from the slag. The inclusions with a radius of 5 μm and 10 μm showed oscillatory behavior. Compared with Figures 7 and 9, the solid inclusions removal ability of slag C3 is improved compared to that of slag A5. Furthermore, the removal time is shorter.

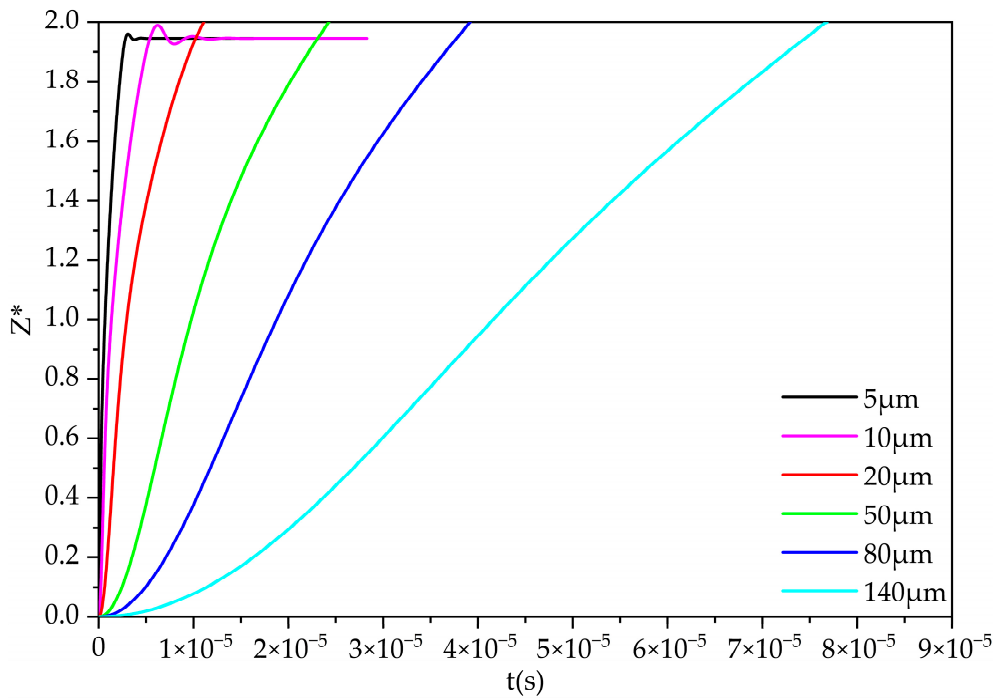

Figure 9. The displacement of solid Al_2O_3 inclusions with different radiuses of inclusions in slag C3.

Similarly, the motion behaviors of inclusions in slag C0–C5 were calculated, and the results are shown in Table 17.

Table 17. Motion behaviors of Al_2O_3 inclusions with different radiuses in slags C0–C5.

	Without Ce_2O_3	**Slags containing Ce_2O_3 in Different Compositions**				
	C0	**C2**	**C1**	**C4**	**C5**	**C3**
Radius	**48%CaO 37.5%Al_2O_3 4.5%SiO_2 10%MgO**	**46.2%CaO 36.3%Al_2O_3 4.5%SiO_2 10%MgO 3%Ce_2O_3**	**45%CaO 37.5%Al_2O_3 4.5%SiO_2 10%MgO 3%Ce_2O_3**	**43.4%CaO 34.1%Al_2O_3 4.5%SiO_2 10%MgO 8%Ce_2O_3**	**45%CaO 32.5%Al_2O_3 4.5%SiO_2 10%MgO 8%Ce_2O_3**	**45%CaO 35.5%Al_2O_3 4.5%SiO_2 10%MgO 5%Ce_2O_3**
5 μm	R	R	R	O	O	O
10 μm	R	O	O	O	O	O
20 μm	R	O	O	P	P	P
30 μm	R	O	P	P	P	P
50 μm	O	P	P	P	P	P
80 μm	O	P	P	P	P	P
140 μm	P	P	P	P	P	P

Note: R = Remain, O = Oscillate, and P = Pass.

The inclusions with a radius of smaller than 10 μm cannot be removed in all of the C series slag systems, and the inclusions with a radius of larger than 20 μm can be removed perfectly in slags C3 to C5. This C series slags showed a better performance than the A series slags for solid inclusion removal.

By comparing the removal of the Al_2O_3 inclusions between slag C0 and slags C1–C5, it can be seen that the refining slag containing rare earth oxide Ce_2O_3 shows a better ability to remove inclusions than ordinary refining slag. The inclusion removal ability of the six slags is ranked as C3 > C5 > C4 > C1 > C2 > C0. By comparing the physical properties of slag C0 and slags C1–C5, it can be found that slags C1–C5 have a higher wettability, as well as a better performance of the wetting effect on the Al_2O_3 inclusion than slag C0. However, the overall wettability varies within a limited range. As shown in Table 3, the viscosity of the six slags is ranked as C3 < C5 < C4 < C1 < C2 < C0. This is the same order as the removal ability of the slags. Thus, the viscosity may be a crucial factor. This is the reason for why the slag containing rare earth oxide Ce_2O_3 shows a better ability to remove Al_2O_3 inclusions.

Compared with Tables 15 and 17, the removal ability of solid Al_2O_3 inclusions in the C series slag system is significantly higher than that in the A series slag system. The limiting size of the inclusions that can be removed is reduced in the C series slag system.

3.4. Discussion

According to the analysis above, the ability of slags containing Ce_2O_3 to remove inclusions is better than the slag without Ce_2O_3, and the viscosity plays a vital role in the ability of the two slag systems to remove inclusions. In the C series slags, the addition of MgO can effectively reduce the viscosity. The sizes of the inclusions that can effectually be removed is related to the statement of the inclusion. In this paper, for solid inclusions, it can be removed with a size of more than 20 μm in a special refining slag with a specific composition. For liquid inclusions, the size of the inclusion needs to be larger than 80 μm. That is to say, the liquid inclusions more easily remain in the molten steel. After the analysis, the ability of the refining slag to remove inclusions of specific compositions can be evaluated.

Nevertheless, the model is used to predict the motion of single particle inclusions at the slag–steel interface in a relatively ideal state, but there are some shortcomings. First, the liquid steel and slag are assumed to be static, without considering the real flow state. Second, the inclusion is a single particle floating at the interface, without considering the collision aggregation between the inclusions. Third, the inclusion may be accelerated and the rising velocity may be higher than the Stokes velocity. Although the results cannot be compared with industrial operations, the integrated model can predict a tendency for the different compositions of the slags. For a specific slag, the composition of the slag could influence the viscosity and surface tension, and further, the overall wettability, and many other issues. In this study, the C series slag with a lower viscosity shows the best performance of inclusion removal. The 45%wt CaO–35.5%wt Al_2O_3–4.5%wt SiO_2–10%wt MgO–5%wt Ce_2O_3 refining slag is optimized in this study. It is noted that a systematic evaluation of the inclusion removal ability of selected slag systems, as well as the effect of the tailored slag on slag eye in ladles [160], are ongoing work.

4. Conclusions

After summarizing and analyzing the motion behaviors of solid and liquid inclusions with different sizes at the steel–slag interface of the two slag systems, the following conclusions can be obtained:

(1) In the refining process, whether solid or liquid inclusions, large inclusions are easier to remove from the steel–slag interface than small inclusions. Reducing the viscosity of the slag is more conducive to the removal of the inclusions. For the same CaO-Ce_2O_3-SiO_2-Al_2O_3 slag system, liquid 50%wtAl_2O_3-50%wtCaO inclusions are more difficult to remove than solid Al_2O_3 inclusions.

(2) The CaO-Ce_2O_3-SiO_2-Al_2O_3-MgO refining slag shows a better ability to remove Al_2O_3 inclusions than that of CaO-SiO_2-Al_2O_3-MgO slag. The reason for this is that the addition of rare earth oxide Ce_2O_3 can decrease the viscosity of slags, as well as improving the wetting effect of slags on Al_2O_3 inclusions.

(3) For two slags systems, the CaO-Ce_2O_3-SiO_2-Al_2O_3-MgO slag system shows a better ability to remove Al_2O_3 inclusions than that of the CaO-Ce_2O_3-SiO_2-Al_2O_3 slag system. The addition of 5% to 8% Ce_2O_3 in the CaO-SiO_2-Al_2O_3-MgO slag is an optimized case for industrial applications.

(4) The integrated model mainly involves an inclusion motion model and the slag properties models, including the interfacial tension, surface tension, and mass action concentration model, based on ion and molecule coexistence theory. However, the predictions are limited to the force balance of inclusions. A combined model considering the transport of inclusions by fluid mechanics, the interaction of inclusions with a turbulent boundary layer, and the movement of inclusions at the steel–slag interface will be a future work.

Author Contributions: Conceptualization, C.C.; methodology, W.L., Y.T., J.D. and C.C.; software, J.C. (Jianqi Cao), Y.L., and C.C.; investigation J.C. (Jianqi Cao), Y.L., F.Z. and C.C.; resources, W.L., Y.T., J.D. and C.C.; data curation, J.C. (Jianqi Cao) and Y.L.; writing—original draft preparation, J.C. (Jianqi Cao) and Y.L.; writing—review and editing, W.L., J.C. (Julong Che), F.Z., Y.T., D.L., J.D. and C.C.; supervision, W.L., J.C. (Julong Che) and C.C.; funding acquisition, C.C. and D.L. All authors have read and agreed to the published version of the manuscript.

Funding: This research was funded by the National Natural Science Foundation of China, grant number 51904204; Research Project Supported by Shanxi Scholarship Council of China, grant number 2022-040; Lyuliang High level Talents Key R&D Project, grant number 2019112; and Scientific and Technological Innovation Programs of Higher Education Institutions in Shanxi, grant numbers 2019L0971, 2019L0938.

Data Availability Statement: Not applicable.

Acknowledgments: The discussions with Professor Keiji Nakajima of KTH-Royal Institute of Technology and Professor Emeritus Shebin Wang of Taiyuan University of Technology are acknowledged. The anonymous reviewers are acknowledged for their valuable comments.

Conflicts of Interest: The authors declare no conflict of interest.

References

1. Kiessling, R. *Non-Metallic Inclusions in Steel: Part III: The Origin and Behavior of Inclusions and Their Influence on the Properties of Steels*; The Metals Society: London, UK, 1968.
2. Zhang, L.F. *Non-Metallic Inclusions in Steels: Fundamentals*; Metallurgical Industry Press: Beijing, China, 2019.
3. Park, J.H.; Zhang, L.F. Kinetic Modeling of Nonmetallic Inclusions Behavior in Molten Steel: A Review. *Metall. Mater. Trans. B* **2020**, *51*, 2453–2482. [CrossRef]
4. Nadif, M.; Lehmann, J.; Burty, M.; Domgin, J.F. Control of Steel Reoxidation and CC Nozzle Clogging: An overview. In Proceedings of the International Conference on Clean Steel 7, Balatonfüred, Hungary, 4–6 June 2007.
5. Huang, R.K.; Zhang, L.F.; Jiang, R.B.; Guo, Y.T.; Zhou, Q.Y.; Duan, H.J. Effect of FeO_x in an ultra-low carbon Al-killed steel on nozzle clogging. *Iron Steel* **2021**, *56*, 43–50. [CrossRef]
6. Hua, C.J.; Wang, M.; Bao, Y.P. Effect of Nozzle Clogging on the Fluid Flow Pattern in a Billet Mold with Particle Image Velocimetry Technology. *Metall. Mater. Trans. B* **2020**, *51*, 2871–2881. [CrossRef]
7. Fu, B.H.; Chen, C.; Cheng, G.G.; Pan, J.X.; Li, Y.; Pan, W. Inclusions in 430 Stainless Steelmaking During AOD-LF-CC Process. *Iron Steel* **2012**, *47*, 40–43. [CrossRef]
8. Chen, C.; Cheng, G.G. Delta-ferrite distribution in a continuous casting slab of Fe-Cr-Mn austenitic stainless steel. *Metall. Mater. Trans. B* **2017**, *48*, 2324–2333. [CrossRef]
9. Li, Y.H.; He, Y.B.; Ren, Z.F.; Bao, Y.P.; Wang, R. Comparative Study of the Cleanliness of Interstitial-Free Steel with Low and High Phosphorus Contents. *Steel Res. Int.* **2021**, *92*, 2000581. [CrossRef]
10. Wang, Y.Z.; Jiang, M.; Wang, X.H. Formation and evolution of inclusions in Q345D steel during secondary reefing process. *Iron Steel* **2022**, *57*, 63–72. [CrossRef]
11. Wang, K.P.; Wang, Y.; Xu, J.F.; Chen, T.J.; Xie, W.; Jiang, M. Investigation on evolution of inclusions in bearing steel during secondary refining. *Iron Steel* **2022**, *57*, 42–49. [CrossRef]
12. Cao, J.Q.; Chen, C.; Xue, L.Q.; Li, Z.; Zhao, J.; Lin, W.M. Analysis of the inclusions in the whole smelting process of non-oriented silicon steel DG47A. *Iron Steel* **2022**. [CrossRef]

13. Yuan, B.H.; Liu, J.H.; Zeng, J.H.; Zhang, M.; Huang, J.H.; Yang, X.D. Evolution of Inclusions and Cleanliness in Ti-Bearing IF Steel Produced via the BOF–LF–RH–CC Process. *Metals* **2022**, *12*, 434. [CrossRef]
14. Yuan, X.B.; Zhong, M.; Wu, Y.W.; Wang, C. Characterizing Inclusions in the Weld Metal of Eh36 Shipbuilding Steel Processed by CaF2-30 Wt Pct TiO_2 Flux. *Metall. Mater. Trans. B* **2022**, *53*, 656–661. [CrossRef]
15. Qiao, T.; Cheng, G.G.; Huang, Y.; Li, Y.; Zhang, Y.L.; Li, Z.C. Formation and Removal Mechanism of Nonmetallic Inclusions in 42CrMo4 Steel during the Steelmaking Process. *Metals* **2022**, *12*, 1505. [CrossRef]
16. Jiang, M.; Liu, J.C.; Li, K.L.; Wang, R.G.; Wang, X.H. Formation Mechanism of Large CaO-SiO_2-Al_2O_3 Inclusions in Si-Deoxidized Spring Steel Refined by Low Basicity Slag. *Metall. Mater. Trans. B* **2021**, *52*, 1950–1954. [CrossRef]
17. Podder, A.; Coley, K.S.; Phillion, A.B. Modeling Study of Steel–Slag–Inclusion Reactions During the Refining of Si–Mn Killed Steel. *Steel Res. Int.* **2022**, 2100831. [CrossRef]
18. Meng, Y.Q.; Li, J.L.; Zhu, H.Y.; Wang, K.P. Effect of LF soft bubbling time on oxide inclusions in Si-killed spring steel. *Iron Steel* **2022**, *57*, 48–54. [CrossRef]
19. Zhang, Y.X.; Chen, C.; Lin, W.M.; Yu, Y.C.; E, D.Y.; Wang, S.B. Numerical Simulation of Tracers Transport Process in Water Model of a Vacuum Refining Unit: Single Snorkel Refining Furnace. *Steel Res. Int.* **2020**, *91*, 2000022. [CrossRef]
20. Ouyang, X.; Lin, W.M.; Luo, Y.; Zhang, Y.Z.; Fan, J.P.; Chen, C.; Cheng, G.G. Effect of Salt Tracer Dosages on the Mixing Process in the Water Model of a Single Snorkel Refining Furnace. *Metals* **2022**, *12*, 1948. [CrossRef]
21. Cheng, G.; Zhang, L.F.; Ren, Y.; Yang, W.; Zhao, X.L.; Wang, G.C. Evolution of Nonmetallic Inclusions with Varied Argon Stirring Condition during Vacuum Degassing Refining of a Bearing Steel. *Steel Res. Int.* **2021**, *92*, 2000364. [CrossRef]
22. Yang, R.G.; Yan, Z.H.; Cao, C.G.; Shi, S.D.; Wang, G.H.; Liu, J.G. Practice of VD furnace oxygen decarburization process. *Iron Steel* **2021**, *56*, 39–43. [CrossRef]
23. Li, Y.H.; Zhu, H.W.; Wang, R.; Ren, Z.F.; Lin, L. Prediction of two phase flow behavior and mixing degree of liquid steel under reduced pressure. *Vacuum* **2021**, *192*, 110480. [CrossRef]
24. Wei, G.S.; Dong, J.F.; Zhu, R.; Han, B.C. Effect of ladle bottom blowing on RH dehydrogenation and inclusions. *Iron Steel* **2021**, *56*, 63–68. [CrossRef]
25. Li, Y.H.; Zhu, H.W.; Wang, R.; Ren, Z.F.; He, Y.B. Bubble behavior and evolution characteristics in the RH riser tube-vacuum chamber. *Int. J. Chem. React. Eng.* **2022**, *20*, 1053–1064. [CrossRef]
26. Zhu, G.S.; Deng, X.X.; Ji, C.X. Effect of vacuum degree on inclusion removal in ultra low carbon steel during RH refining process. *Iron Steel* **2022**. [CrossRef]
27. Wang, K.P.; Wang, Y.; Xu, J.F.; Xie, W.; Chen, T.J.; Jiang, M. Influence of Temperature Drop from 1773 K (1500 °C) to 1743 K (1470 °C) on Inclusion of High Carbon Chromium Bearing Steel Melts Treated by RH Vacuum Degassing. *Metall. Mater. Trans. B* **2022**. [CrossRef]
28. Wang, Q.; Tan, C.; Huang, A.; Yan, W.; Gu, H.Z.; He, Z.; Li, G.Q. Numerical simulation on refractory wear and inclusion formation in continuous casting tundish. *Metall. Mater. Trans. B* **2021**, *52*, 1344–1356. [CrossRef]
29. Chang, S.; Zou, Z.S.; Li, B.K.; ISAC, M.; Guthrie, R.I.L. Modeling Inclusion Removal when Using Microbubble Swarm in a Full-Scale Tundish with an Impact Pad. *Metall. Mater. Trans. B* **2021**, *53*, 526–536. [CrossRef]
30. Xin, Z.Y.; Cui, H.N.; Li, T.; Tang, G.Z.; Zhu, Y.L.; Yan, J.C.; Li, J.G. Numerical Simulation of Inclusion Removal by Bubble Injection in the Submerged Nozzle With Swirling Flow. *Metall. Mater. Trans. B* **2022**, *53*, 2570–2586. [CrossRef]
31. Fan, J.P.; Li, Y.Q.; Chen, C.; Ouyang, X.; Wang, T.Y.; Lin, W.M. Effect of Uniform and Non-Uniform Increasing Casting Flow Rate on Dispersion and Outflow Percentage of Tracers in Four Strand Tundishes under Strand Blockage Conditions. *Metals* **2022**, *12*, 1016. [CrossRef]
32. Reis, B.H.; Bielefeldt, W.V.; Vilela, A.C.F. Absorption of non-metallic inclusions by steelmaking slags—A review. *J. Mater. Res. Technol.* **2014**, *3*, 179–185. [CrossRef]
33. Wang, R.; Li, Y.H.; Li, D.Z.; Kang, Y.; Bao, Y.P.; Yan, Z.J. Inclusions Absorbed by Slags in Interstitial-Free Steel Production. *Steel Res. Int.* **2020**, *91*, 1900440. [CrossRef]
34. Wen, X.; Ren, Y.; Zhang, L.F. Effect of CaF2 Contents in Slag on Inclusion Absorption in a Bearing Steel. *Steel Res. Int.* **2022**, 2200218. [CrossRef]
35. Salgado, U.D.; Weiß, C.; Michelic, S.K.; Bernhard, C. Fluid force-induced detachment criteria for nonmetallic inclusions adhered to a refractory/molten steel interface. *Metall. Mater. Trans. B* **2018**, *49*, 1632–1643. [CrossRef]
36. Wikström, J.; Nakajima, K.; Jonsson, L.; Jönsson, P. Application of a Model for Liquid Inclusion Separation at a Steel-Slag Interface for Laboratory and Industrial Situations. *Steel Res. Int.* **2008**, *79*, 826–834. [CrossRef]
37. Chen, C.; Cheng, G.G.; Yang, H.K.; Hou, Z.B. Physical modeling of Fluid flow Characteristics in a Delta Shaped, Four-Strand Continuous Casting Tundish with Different Flow Control Devices. *Adv. Mater. Res.* **2011**, *284–286*, 1071–1079. [CrossRef]
38. Chen, C.; Cheng, G.G.; Sun, H.B.; Hou, Z.B.; Wang, X.C.; Zhang, J.Q. Effects of salt tracer amount, concentration and kind on the fluid flow behavior in a hydrodynamic model of continuous casting tundish. *Steel Res. Int.* **2012**, *83*, 1141–1151. [CrossRef]
39. Chen, C.; Rui, Q.X.; Cheng, G.G. Effect of salt tracer amount on the mixing time measurement in a hydrodynamic model of gas-stirred ladle system. *Steel Res. Int.* **2013**, *84*, 900–907. [CrossRef]
40. Conejo, A.N.; Zhao, G.A.; Zhang, L.F. On the Limits of the Geometric Scale Ratio Using Water Modeling in Ladles. *Metall. Mater. Trans. B* **2021**, *52*, 2263–2274. [CrossRef]
41. Yang, R.W.; Chen, C.; Lin, Y.C.; Zhao, Y.; Zhao, J.; Zhu, J.J.; Yang, S.S. Water model experiment on motion and melting of scarp in gas stirred reactors. *Chin. J. Process Eng.* **2022**, *22*, 954–962. [CrossRef]

42. Pei, K.H.; Chen, C.; Zhao, Y.; Lin, Y.C.; Yang, R.W.; Zhu, J.J.; Wang, T.; Yang, K.; Lin, W.M. Water model experiment on the motion, melting, and mixing of scrap in bottom stirred reactors. *Chin. J. Process Eng.* **2022**, *22*, 1601–1612. [CrossRef]
43. Lindborg, U.; Torssell, K. A Collision Model for the Growth and Separation of Deoxidation Products. *Trans. Metall. Soc. AIME* **1968**, *242*, 94–102.
44. Linder, S. Hydrodynamics and Collisions of Small Particles in a Turbulent Metallic Melt with Special Reference to Deoxidation of Steel. *Scand. J. Metall.* **1974**, *3*, 137–150.
45. Engh, T.A.; Lindskog, N. A Fluid Mechanical Model of Inclusion Removal. *Scand. J. Metall.* **1975**, *4*, 49–58.
46. Söder, M.; Jönsson, P.; Alexis, J. Most relevant mechanisms of inclusion growth in an induction-stirred ladle. *Scand. J. Metall.* **2002**, *31*, 210–220. [CrossRef]
47. Lei, H.; Nakajima, K.; He, J.C. Mathematical Model for Nucleation, Ostwald Ripening and Growth of Inclusion in Molten Steel. *ISIJ Int.* **2010**, *50*, 1735–1745. [CrossRef]
48. Nakanishi, K.; Szekely, J. Deoxidation Kinetics in a Turbulent Flow Field. *Trans. ISIJ* **1975**, *15*, 522–530. [CrossRef]
49. Johansen, S.T.; Boysan, F.; Engh, T.A. Numerical calculations of removal of inclusions and dissolution of refractory in bubble stirred ladles. In Proceedings of the 4th Japan-Nordic Countries Joint Symposiums on Science and Technology of Process Metallurgy, Tokyo, Japan; 1986; pp. 182–215.
50. Miki, Y.; Shimada, Y.; Thomas, B.G.; Denissov, A. Model of Inclusion Removal during RH Degassing of Steel. *Iron Steelmak.* **1997**, *28*, 31–38. Available online: https://experts.illinois.edu/en/publications/model-of-inclusion-removal-during-rh-degassing-of-steel (accessed on 19 January 2023).
51. Wakoh, M.; Fuchigama, K.; Endoh, K.; Imamura, N.; Kiyose, A.; Sawada, I. Analysis of Inclusion Behavior in a ladle refining process by using newly developed coagulation model. In Proceedings of the Scanmet I, Luleå, Sweden, 7–8 June 1999; pp. 267–274.
52. Sheng, D.Y.; Söder, M.; Jönsson, P.; Jonsson, L. Modeling micro-inclusion growth and separation in gas-stirred ladles. *Scand. J. Metall.* **2002**, *31*, 134–147. [CrossRef]
53. Söder, M.; Jönsson, P.; Jonsson, L. Inclusion growth and removal in gas-stirred ladles. *Steel Res. Int.* **2004**, *75*, 128–138. [CrossRef]
54. Hallberg, M.; Jönsson, P.G.; Jonsson, L.T.I.; Eriksson, R. Process model of inclusion separation in a stirred steel ladle. *Scand. J. Metall.* **2005**, *34*, 41–56. [CrossRef]
55. Kwon, Y.J.; Zhang, J.; Lee, H.G. A CFD-based Nucleation-growth-removal Model for Inclusion Behavior in a Gas-agitated Ladle during Molten Steel Deoxidation. *ISIJ Int.* **2008**, *48*, 891–900. [CrossRef]
56. Geng, D.Q.; Lei, H.; He, J.C. Numerical Simulation for Collision and Growth of Inclusions in Ladles Stirred with Different Porous Plug Configurations. *ISIJ Int.* **2010**, *50*, 1597–1605. [CrossRef]
57. Claudotte, L.; Rimbert, N.; Gardin, P.; Simonnet, M.; Lehmann, L.; Oesterlé, B. Behaviour of Oxide Inclusions in Liquid Steel Multi-QMOM Simulation. *Steel Res. Int.* **2010**, *81*, 630–636. [CrossRef]
58. Daoud, I.L.A.; Rimbert, N.; Jardy, A.; Oesterlé, B.; Hans, S.; Bellot, J.P. 3D modeling of the aggregation of oxide inclusions in a liquid steel ladle: Two numerical approaches. *Adv. Eng. Mater.* **2011**, *13*, 543–549. [CrossRef]
59. Gardin, P.; Gauthier, S.; Simonnet, M.; Lehmann, J. Multiphase Model for Predicting the Elimination of Inclusions inside a Liquid-Steel Ladle. *Adv. Eng. Mater.* **2011**, *13*, 538–542. [CrossRef]
60. Lou, W.T.; Zhu, M.Y. Numerical simulations of inclusion behavior in gas-stirred ladles. *Metall. Mater. Trans. B* **2013**, *44*, 762–782. [CrossRef]
61. Chen, C.; Jonsson, L.T.I.; Tilliander, A.; Cheng, G.G.; Jönsson, P.G. A mathematical modeling study of tracer mixing in a continuous casting tundish. *Metall. Mater. Trans. B* **2015**, *46*, 169–190. [CrossRef]
62. Chen, C.; Jonsson, L.T.I.; Tilliander, A.; Cheng, G.G.; Jönsson, P.G. A mathematical modeling study of the influence of small amounts of KCl solution tracers on mixing in water and residence time distribution of tracers in a continuous flow reactor-metallurgical tundish. *Chem. Eng. Sci.* **2015**, *137*, 914–937. [CrossRef]
63. Guo, X.P.; Godinez, J.; Walla, N.J.; Silaen, A.K.; Oltmann, H.; Thapliyal, V.; Bhansali, A.; Pretorius, E.; Zhou, C.Q. Computational Investigation of Inclusion Removal in the Steel-Refining Ladle Process. *Processes* **2021**, *9*, 1048. [CrossRef]
64. Wang, F.; Sun, B.Y.; Liu, Z.Q.; Li, B.K.; Huang, S.; Zhang, B.J. Numerical Simulation on Motion Behavior of Inclusions in the Lab-Scale Electroslag Remelting Process with a Vibrating Electrode. *Metals* **2021**, *11*, 1784. [CrossRef]
65. Siddiqui, M.I.H.; Albaqami, A.; Arifudin, L.; Alluhydan, K.; Alnaser, I.A. Simulation of Inclusion Particle Motion Behavior under Interfacial Tension in Continuous Casting Mold. *Materials* **2022**, *15*, 7458. [CrossRef]
66. Chen, C.; Ni, P.Y.; Jonsson, L.T.I.; Tilliander, A.; Cheng, G.G.; Jönsson, P.G. A Model Study of Inclusions Deposition, Macroscopic Transport, and Dynamic Removal at Steel–Slag Interface for Different Tundish Designs. *Metall. Mater. Trans. B* **2016**, *47*, 1916–1932. [CrossRef]
67. Tacke, K.H.; Ludwig, J.C. Steel flow and inclusion separation in continuous casting tundishes. *Steel Res.* **1987**, *58*, 262–270. [CrossRef]
68. Rückert, A.; Warzecha, M.; Koitzsch, R.; Pawlik, M.; Pfeifer, H. Particle Distribution and Separation in Continuous Casting Tundish. *Steel Res. Int.* **2009**, *80*, 568–574. [CrossRef]
69. Gutiérrez, E.; Garcia-Hernandez, S.; Barreto, J.J. Mathematical Analysis of the Touching Inclusions Parameters at the Tundish Free Surface to Predict More Realistic Inclusion Removal Rates. *Steel Res. Int.* **2019**, *90*, 1900328. [CrossRef]
70. Chen, C. Some Aspects on Macroscopic Mixing in a Tundish. Ph.D. Thesis, KTH Royal Institute of Technology, Stockholm, Sweden, 2015.

71. Nakajima, K.; Okamura, K. Inclusion Transfer Behavior across Molten Steel-Slag Interface. In Proceedings of the 4th International Conference on Molten Slags and Fluxes, Sendai, Japan, 8–11 June 1992; pp. 505–510.
72. Bouris, D.; Bergeles, G. Investigation of Inclusion Re-Entrainment from the Steel-Slag Interface. *Metall. Mater. Trans. B* **1998**, *29*, 641–649. [CrossRef]
73. Strandh, J.; Nakajima, K.; Eriksson, R.; Jönsson, P. Solid inclusion transfer at a steel-slag interface with focus on tundish conditions. *ISIJ Int.* **2005**, *45*, 1597–1606. [CrossRef]
74. Strandh, J.; Nakajima, K.; Eriksson, R.; Jönsson, P. A mathematical model to study liquid inclusion behavior at the steel-slag interface. *ISIJ Int.* **2005**, *45*, 1838–1847. [CrossRef]
75. Xuan, C.; Persson, E.S.; Sevastoplev, R.; Nzotta, M. Motion and detachment behaviors of liquid inclusion at molten steel-slag interfaces. *Metall. Mater. Trans. B* **2019**, *50*, 1957–1973. [CrossRef]
76. Shannon, G.N.; Sridhar, S. Modeling Al_2O_3 inclusion separation across steel-slag interfaces. *Scand. J. Metall.* **2005**, *34*, 353–362. [CrossRef]
77. Shannon, G.N.; Sridhar, S. Film-Drainage, Separation and Dissolution of $A1_2O_3$ Inclusions across Interfaces between Molten Steel and Ladle-, Tundish- and Mold-Slags. *High Temp. Mater. Proc.* **2005**, *24*, 111–124. [CrossRef]
78. Zhou, Y.L.; Deng, Z.Y.; Zhu, M.Y. Consideration on removal of non-spherical solid inclusions at slag-steel interface. *Chin. J. Process Eng.* **2022**, *22*, 222–231. [CrossRef]
79. Valdez, M.; Shannon, G.S.; Sridhar, S. The Ability of Slags to Absorb Solid Oxide Inclusions. *ISIJ Int.* **2006**, *46*, 450–457. [CrossRef]
80. Shannon, G.; White, L.; Sridhar, S. Modeling inclusion approach to the steel/slag interface. *Mater. Sci. Eng. A* **2008**, *495*, 310–315. [CrossRef]
81. Liu, C.; Yang, S.F.; Li, J.S.; Zhu, L.B.; Li, X.G. Motion Behavior of Nonmetallic Inclusions at the Interface of Steel and Slag. Part I: Model Development, Validation, and Preliminary Analysis. *Metall. Mater. Trans. B* **2016**, *47*, 1882–1892. [CrossRef]
82. Yang, S.F.; Li, J.S.; Liu, C.; Sun, L.Y.; Yang, H.B. Motion Behavior of Nonmetallic Inclusions at the Interface of Steel and Slag. Part II: Model Application and Discussion. *Metall. Mater. Trans. B* **2014**, *45*, 2453–2463. [CrossRef]
83. Liu, W.; Yang, S.F.; Li, J.S. Calculation of Static Suspension Depth and Meniscus Shape of a Solid Spherical Inclusion at the Steel–Slag Interface. *Metall. Mater. Trans. B* **2020**, *51*, 422–425. [CrossRef]
84. Liu, W.; Liu, J.; Zhao, H.X.; Yang, S.F.; Li, J.S. CFD Modeling of Solid Inclusion Motion and Separation from Liquid Steel to Molten Slag. *Metall. Mater. Trans. B* **2021**, *52*, 2430–2440. [CrossRef]
85. Zhang, X.M.; Pirker, S.; Saeedipour, M. Numerical investigation of particle motion at the steel–slag interface in continuous casting using VOF method and dynamic overset grids. *Exp. Comput. Multiph. Flow* **2023**, *5*, 178–191. [CrossRef]
86. Du, Y.N.; Guo, L.; Yang, Y.; Zhang, S.; Yu, H.Z.; Guo, Z.C. Numerical simulation of inclusions floating behavior under supergravity field in liquid steel. *Iron Steel* **2022**, *57*, 54–62. [CrossRef]
87. Liu, Y.Q.; Wang, L.J.; Chou, K.C. Dissolution Behavior of Al_2O_3 in Refining Slags Containing Ce_2O_3. *ISIJ Int.* **2014**, *54*, 728–733. [CrossRef]
88. Wang, L.J.; Wang, Q.; Li, J.M.; Chou, K.C. Dissolution mechanism of Al_2O_3 in refining slags contained Ce_2O_3. *J. Min. Metall. Sect. B-Metall.* **2016**, *52*, 35–40. [CrossRef]
89. Shi, G.Y.; Zhang, T.A.; Dou, Z.H.; Niu, L.P. Dissolution Behavior of Al_2O_3 Inclusions in CaO-Al_2O_3 Based Slag Representing Aluminothermic Reduction Slag. *Crystals* **2020**, *10*, 1061. [CrossRef]
90. Zhao, S.; Li, Z.S.; Xu, R.Z.; Khasraw, D.; Song, G.Y.; Xu, D. Dissolution Behavior of Different Inclusions in High Al Steel Reacted with Refining Slags. *Metals* **2021**, *11*, 1801. [CrossRef]
91. Yeo, S.; Um, H.; Chung, Y. The Effect of Alumina Activity on Dissolution Behavior of Alumina Particles in CaO-Al_2O_3-SiO_2 Slags. *Metall. Mater. Trans. B* **2021**, *52*, 3938–3945. [CrossRef]
92. Ren, C.Y.; Zhang, L.F.; Zhang, J.; Wu, S.J.; Zhu, P.; Ren, Y. In Situ Observation of the Dissolution of Al_2O_3 Particles in CaO-Al_2O_3-SiO_2 Slags. *Metall. Mater. Trans. B* **2021**, *52*, 3288–3301. [CrossRef]
93. Song, S.Y.; Li, J.; Yan, W. Dissolution mechanism of alumina inclusions into CaO–SiO_2–Al_2O_3–Fe_tO–MgO slag via a converter tapping process. *Int. J. Appl. Ceram. Technol.* **2022**, *19*, 2734–2748. [CrossRef]
94. Zhang, L.F.; Ren, Y. Concept of inclusion capacity of slag and its application. *Iron Steel* **2022**. [CrossRef]
95. Xuan, C.J.; Mu, W.Z. A phase-field model for the study of isothermal dissolution behavior of alumina particles into molten silicates. *J. Am. Ceram. Soc.* **2019**, *102*, 6480–6497. [CrossRef]
96. Xuan, C.J.; Mu, W.Z. A mechanism theory of dissolution profile of oxide particles in oxide melt. *J. Am. Ceram. Soc.* **2020**, *104*, 57–75. [CrossRef]
97. Mu, W.Z.; Xuan, C.J. Phase-field study of dissolution behaviors of different oxide particles into oxide melts. *Ceram. Int.* **2020**, *46*, 14949–14956. [CrossRef]
98. Xuan, C.J.; Mu, W.Z. Dissolution kinetics of arbitrarily-shaped alumina in oxide melt: An integration of phase-field modelling and real-time observation study. *J. Alloys Compd.* **2020**, *834*, 155168. [CrossRef]
99. Pan, X.Y.; Shen, F.M.; Gao, Q.J.; Jiang, X.; Zheng, H.Y. Effect of Erosion Behavior of FeO-CaO-SiO_2-MgO-Al_2O_3 Blast Furnace Primary Slag on Al_2O_3 Substrate. *Crystals* **2021**, *11*, 957. [CrossRef]
100. Zheng, H.Y.; Wang, S.; Guo, Y.C.; Jiang, X.; Gao, Q.J.; Shen, F.M. Thermodynamic model for calculating sulfur distribution ratio between CaO-SiO_2-MgO-Al_2O_3 slag and hot metal. *Iron Steel* **2021**, *56*, 16–23. [CrossRef]

101. Hu, X.G.; Shen, F.M.; Zheng, H.Y.; Guo, Y.C.; Jiang, X.; Gao, Q.J. Effect of temperature on Al_2O_3 activity in CaO-SiO_2-Al_2O_3-MgO blast furnace slag system. *Iron Steel* **2022**, *57*, 25–33. [CrossRef]
102. Liu, K.; Han, Y.H.; Yang, F.; Zhu, L.G. Effect of MgO on microstructure of CaO-Al_2O_3 based quaternary system mold fluxes. *Iron Steel* **2020**, *55*, 52–58. [CrossRef]
103. Zhao, B.B.; Zhang, J.; Yan, B.J. Interfacial Phenomena and Reaction Kinetics between High Al Molten Steel and CaO-SiO_2-Type Flux. *Metals* **2022**, *12*, 391. [CrossRef]
104. Wang, X.F.; Wang, Q.Q.; Zhang, X.B.; Wang, Q.; He, S.P. Effect of AlN on properties of CaO-SiO_2 based mold fluxes for high-Al steel. *Iron Steel* **2022**, *57*, 64–71. [CrossRef]
105. Silva, A.M.B.; Oliveira, M.A.; Peixoto, J.J.M.; Silva, C.A.D. Slag-Steel Emulsification on a Modified RH Degasser. *Metall. Mater. Trans. B* **2021**, *52*, 2111–2126. [CrossRef]
106. Li, S.J.; Cheng, G.G.; Yang, L.; Chen, L.; Yan, Q.Z.; Li, C.W. A Thermodynamic Model to Design the Equilibrium Slag Compositions during Electroslag Remelting Process: Description and Verification. *ISIJ Int.* **2017**, *4*, 713–722. [CrossRef]
107. Bublik, S.; Tangstad, M.; Einarsrud, K.R.E. Interfacial Behaviour in Ferroalloys: The Influence of FeMn Slag Composition. *Metall. Mater. Trans. B* **2022**, *53*, 3276–3291. [CrossRef]
108. Bai, C.G.; Yan, Z.M.; Pang, Z.D.; Jiang, Y.Y.; Ling, J.W.; Lü, X.W. Advances of measurement and calculation model of slag viscosity. *Iron Steel* **2020**, *55*, 27–37. [CrossRef]
109. Lü, X.W.; Yan, Z.M.; Pang, Z.D.; Bai, C.G.; Liang, D.; Xie, H. Effect of Al_2O_3 on physicochemical properties and structure of blast furnace slag: Review. *Iron Steel* **2020**, *55*, 1–10. [CrossRef]
110. Fang, J.L.; Pang, Z.G.; Xing, X.D.; Xu, R.S. Thermodynamic Properties, Viscosity, and Structure of CaO–SiO_2–MgO–Al_2O_3–TiO_2–Based Slag. *Materials* **2021**, *14*, 124. [CrossRef]
111. Haghdani, S.; Tangstad, M.; Einarsrud, K.R.E. A Raman-Structure Model for the Viscosity of SiO_2-CaO-Al_2O_3 System. *Metall. Mater. Trans. B* **2022**, *53*, 1733–1746. [CrossRef]
112. Zhang, R.; Meng, Y.F.; Wang, Z.; Jiao, S.Y.; Jia, J.X.; Min, Y.; Liu, C.J. Surface Tension Prediction of Multicomponent Slags of the CaO–SiO_2–Al_2O_3–FeO–Fe_2O_3 System Based on Microstructure Analysis. *Metall. Mater. Trans. B* **2022**, *53*, 571–583. [CrossRef]
113. Wang, L.; Cheng, S.S.; Liu, P.B.; Chen, Y.B. Effect of K_2O and Na_2O on activity of components and MgO content of high Al_2O_3 slag. *Iron Steel* **2022**, *57*, 48–56. [CrossRef]
114. Zhao, M.G.; Li, G.; Li, Z.; Wang, Q.Q.; He, S.P. Study of Thermodynamic for Low-Reactive CaO-BaO-Al_2O_3-SiO_2-CaF_2-Li_2O Mold Flux Based on the Model of Ion and Molecular Coexistence Theory. *Metals* **2022**, *12*, 1099. [CrossRef]
115. He, S.P.; Chen, G.J.; Guo, Y.T.; Shen, B.Y.; Wang, Q. Morphology control for Al_2O_3 inclusions without Ca treatment in high aluminum steel. *Metall. Mater. Trans. B* **2015**, *46*, 585–594. [CrossRef]
116. Hasegawa, M.; Sakuma, K. Use of Rare Earth Elements in Steel Making. *Tetsu-to-Hagané* **1956**, *42*, 503–517. [CrossRef]
117. Malm, S. On the Precipitation of Slag Inclusions during Solidification of High-carbon Steels Deoxidized with Aluminium and Misch Metal. *Scand. J. Metall.* **1976**, *5*, 248–257.
118. Emi, T.; Haida, O.; Sakuraya, T.; Sanbongi, K. Mechanism of sulfides precipitation during solidification of calcium- and rare earth treated ingots. In Proceedings of the Steelmaking Proceedings, Detroit, MI, USA; 1979; Volume 62, pp. 574–584.
119. Zhao, S.; Han, Q.; Shen, F.; Shao, G.; Xie, Z. Study on the Nozzle Blockage Mechanism of Steel Containing Rare Earth Metals during Casting. *Scand. J. Metall.* **1985**, *14*, 175–182.
120. Mizuno, M.; Berjoan, R.; Coutures, J.P.; Foex, M. Phase Diagram of the System Al_2O_3-La_2O_3 at Elevated Temperature. *Yogyo-Kyokai-Shi* **1974**, *82*, 631–636. [CrossRef]
121. Mizuno, M.; Berjoan, R.; Coutures, J.P.; Foex, M. Phase Diagram of the System Al_2O_3-CeO_2 at Liquidus Temperature. *Yogyo-Kyokai-Shi* **1975**, *83*, 90–96. [CrossRef]
122. Ueda, S.; Morita, L.; Sano, N. Activity of $AlO_{1.5}$ for the CaO–$AlO_{1.5}$–$CeO_{1.5}$ System at 1773 K. *ISIJ Int.* **1998**, *38*, 1292–1296. [CrossRef]
123. Wu, P.; Pelton, A.D. Coupled thermodynamic-phase diagram assessment of the rare earth oxide-aluminium oxide binary systems. *J. Alloys Compd.* **1992**, *179*, 259–287. [CrossRef]
124. Navrotsky, A.; Lee, W.; Mielewczyk-Gryn, A.; Ushakov, S.V.; Anderko, A.; Wu, H.H.; Riman, R.E. Thermodynamics of solid phases containing rare earth oxides. *J. Chem. Thermodyn.* **2015**, *88*, 126–141. [CrossRef]
125. Sun, L.F.; Liu, Z.Y.; Jiang, M.F. Phase Equilibria of CaO-SiO_2-La_2O_3-Nb_2O_5 System in Reducing Atmosphere. *Metals* **2022**, *12*, 768. [CrossRef]
126. Jeong, S.J.; Kim, T.S.; Park, J.H. Relationship Between Sulfide Capacity and Structure of MnO-SiO_2-Al_2O_3-Ce_2O_3 System. *Metall. Mater. Trans. B* **2017**, *48*, 545–553. [CrossRef]
127. Qi, J.; Liu, C.J.; Zhang, C.; Jiang, M.F. Effect of Ce_2O_3 on Structure, Viscosity, and Crystalline Phase of CaO-Al_2O_3-Li_2O-Ce_2O_3 Slags. *Metall. Mater. Trans. B* **2017**, *48*, 11–16. [CrossRef]
128. Ma, Z.; Zhao, Z.W.; Guo, W.T.; Wang, Z. Influence of Nb_2O_5 and basicity on the viscosity and structure of CaO-SiO_2-Nb_2O_5-CeO_2-CaF_2 slag system. *Metall. Res. Technol.* **2020**, *117*, 307. [CrossRef]
129. Wu, C.C.; Cheng, G.G.; Long, H. Calculating model of action concentration of slag systems containing Ce_2O_3. *Chin. J. Nonferrous Met.* **2013**, *23*, 2999–3005. [CrossRef]

130. Wu, C.C.; Cheng, G.G.; Long, H.; Yang, X.H. A Thermodynamic Model for Evaluation of Mass Action Concentrations of Ce_2O_3-contained Slag Systems Based on the Ion and Molecule Coexistence Theory. *High Temp. Mater. Proc.* **2013**, *32*, 207–214. [CrossRef]
131. Wu, C.C.; Cheng, G.G.; Tian, J. A Thermodynamic Model for Evaluation of Mass Action Concentrations of La_2O_3-Al_2O_3-CaF_2-CaO-MgO Slags for Electroslag Remelting Based on the Ion and Molecule Coexistence Theory. *High Temp. Mater. Proc.* **2013**, *32*, 541–550. [CrossRef]
132. Wu, C.C.; Cheng, G.G.; Long, H. Effect of Ce_2O_3 and CaO/Al_2O_3 on the Phase, Melting Temperature and Viscosity of CaO-Al_2O_3-10 Mass% SiO_2 Based Slags. *High Temp. Mater. Proc.* **2014**, *33*, 77–84. [CrossRef]
133. Long, H.; Cheng, G.G.; Wu, B.; Wu, Y. Melting and Fluidity Properties of Refining Slag Containing Ce_2O_3 for Steelmaking. *J. Chin. Rare Earth Soc.* **2010**, *28*, 721–727. Available online: http://www.re-journal.com/WKD3/WebPublication/paperDigest.aspx?paperID=28ff3254-3d8b-4c9d-83fc-f0ff6e2f874b (accessed on 20 November 2022).
134. Wu, C.C.; Cheng, G.G. Calculating models on surface tension of RE_2O_3-MgO-SiO_2 (RE = La, Nd, Sm, Gd and Y) melts. *Trans. Nonferrous Met. Soc. China* **2014**, *24*, 3696–3701. [CrossRef]
135. Yang, X.H.; Long, H.; Cheng, G.G.; Wu, C.C.; Wu, B. Effect of refining slag containing Ce_2O_3 on steel cleanliness. *J. Rare Earths* **2011**, *29*, 1079–1083. [CrossRef]
136. Wu, C.C. Research on the Rare Earth Addition Technology and Theory in Refining Process for Special Steel. Ph.D. Thesis, University of Science and Technology Beijing, Beijing, China, 2015.
137. Babenko, A.A.; Smirnov, L.A.; Upolovnikova, A.G.; Shartdinov, R.R. Study of possibility of cerium reduction from slags of CaO-SiO_2-Ce_2O_3-15%Al_2O_3-8%MgO system. *IOP Conf. Ser. Mater. Sci. Eng.* **2020**, *966*, 012010. [CrossRef]
138. Li, D.Z.; Wang, P.; Chen, X.Q.; Fu, P.X.; Luan, Y.K.; Hu, X.Q.; Liu, H.W.; Sun, M.Y.; Chen, Y.; Cao, Y.F.; et al. Low-oxygen rare earth steels. *Nat. Mater.* **2022**, *21*, 1137–1143. [CrossRef]
139. Kang, J.; Yu, Y.C.; Zhang, J.L.; Chen, C.; Wang, S.B. Effect of Rare Earth on Inclusion Evolution in Industrial Production of HRB500E Steel. *Metall. Res. Technol.* **2021**, *118*, 220. [CrossRef]
140. Wang, H.; Bao, Y.P.; Zhi, J.G.; Duan, C.Y.; Gao, S.; Wang, M. Effect of Rare Earth Ce on the Morphology and Distribution of Al_2O_3 Inclusions in High Strength IF Steel Containing Phosphorus during Continuous Casting and Rolling Process. *ISIJ Int.* **2021**, *61*, 657–666. [CrossRef]
141. Zhang, J.; Ren, Y.; Ren, Q.; Zhang, L.F. Transient Evolution of Nonmetallic Inclusions in a Si–Mn-Killed Stainless Steel with Cerium Addition. *Steel Res. Int.* **2022**, *93*, 2100773. [CrossRef]
142. Yang, H.X.; Ren, Y.; Ji, S.; Zhang, L.F. Modification of Sulfides in a High Sulfur Steel by Cerium Addition. *Metall. Mater. Trans. B* **2022**. [CrossRef]
143. Bao, D.H.; Cheng, G.G.; Huang, Y.; Qiao, T.; Dai, W.X. Refinement of Solidification Structure of H13 Steel by Rare Earth Sulfide. *Steel Res. Int.* **2022**, *93*, 2100304. [CrossRef]
144. Liu, D.Q.; Liu, M.; Jiang, X.; Yu, Y.H.; Zhang, Z.M.; Feng, X.M.; Lai, C.B. Effect of Yttrium-Based Rare Earth on Inclusions and Cryogenic Temperature Impact Properties of Offshore Engineering Steel. *Crystals* **2022**, *12*, 305. [CrossRef]
145. Jiang, Y.Y.; Li, Y.C.; Dai, Q.W.; Chai, S.S.; Li, K.J. Evolution of inclusions with cerium addition and effects of C-containing rare earth inclusions on the toughness of ultra-high-strength structural steel. *Ironmak. Steelmak.* **2022**, 2099696. [CrossRef]
146. Huang, F.; Li, J.; Geng, R.M.; Wang, C.C. Effect of rare earth on inclusion evolution and corrosion resistance of HRB400E steel. *Mater. Corros.* **2022**, 13104. [CrossRef]
147. Zhang, J. *Computational Thermodynamics of Metallurgical Melt and Solutions*, 1st ed.; Metallurgical Industry Publisher: Beijing, China, 2007; p. 7.
148. Cheng, G.G.; Liao, N.B. Calculation Model for Surface Tension of Slag Melt. *J. Iron Steel Res. Int.* **1999**, *6*, 17–20. Available online: https://kns.cnki.net/KCMS/detail/detail.aspx?dbcode=CJFD&filename=YING199902004 (accessed on 20 November 2022).
149. Zhou, Y.; Zhu, R.; Wang, H.Y.; Zhang, H.J. Effect of various components on the distribution of phosphorus in CaO–FeO–MgO–SiO_2–MnO–TiO_2–V_2O_5–P_2O_5 slag based on IMCT. *Ironmak. Steelmak.* **2021**, *48*, 570–578. [CrossRef]
150. Li, B.; Li, L.; Guo, H.J.; Guo, J.; Duan, S.C.; Sun, W.X. A phosphorus distribution prediction model for CaO–SiO_2–MgO–FeO–Fe_2O_3–Al_2O_3–P_2O_5 slags based on the IMCT. *Ironmak. Steelmak.* **2020**, *47*, 771–780. [CrossRef]
151. Zhang, G.L.; Cheng, G.G.; Wang, Y.P.; Zhang, X.; Tan, B.; Yuan, C.W.; Miao, H.S. A thermodynamic model of the titanium distribution behaviour between slag and molten steel during LF refining process: Description and application. *Ironmak. Steelmak.* **2022**, *49*, 679–692. [CrossRef]
152. Sun, H.; Yang, J.; Yang, W.K.; Zhang, R.H. Evaluation of Phosphorus Enrichment Capacity of CaO–SiO_2–FeO–MgO–MnO–P_2O_5–Al_2O_3 Dephosphorization Slag Based on Ion-Molecule Coexistence Theory. *Steel Res. Int.* **2022**, 2200662. [CrossRef]
153. Butler, J.A.V. The Thermodynamics of the Surfaces of Solutions. *Roy. Soc.* **1932**, *135*, 348–375. [CrossRef]
154. Wu, C.C.; Cheng, G.G.; Ma, Q.Q. Calculation model of Surface Tension of CaF_2-CaO-Al_2O_3-MgO-SiO_2 Slag System. *Shanghai Metals* **2014**, *36*, 33–36, 41. [CrossRef]
155. Wu, C.C.; Cheng, G.G. Calculating Models on the Surface Tension of CaO-Al_2O_3-TiO_2 Molten Slag. *Shanghai Metals* **2014**, *36*, 35–39. [CrossRef]
156. Wu, C.C.; Cheng, G.G. Computational Model on Surface Tension of CaO-MnO-SiO_2 Slag System. *Hot Work. Technol.* **2014**, *43*, 58–62. [CrossRef]

157. Girifalco, L.A.; Good, R.J. A theory for the estimation of surface and interfacial energies. I. Derivation and application to interfacial tension. *J. Phys. Chem.* **1957**, *61*, 904–909. [CrossRef]
158. Nakajima, K. Estimation of Interfacial Tensions between Phases in the Molten Iron-Slag-Inclusion (Alumina) System. *Tetsu-to-Hagané* **1994**, *80*, 383–388. [CrossRef]
159. Yang, H.B. Study on Moving Behavior of Inclusion during Process of Passing Steel-Slag Interface. Ph.D. Thesis, University of Science and Technology Beijing, Beijing, China, 2015.
160. Conejo, A.N.; Feng, W.H. Ladle Eye Formation Due to Bottom Gas Injection: A Reassessment of Experimental Data. *Metall. Mater. Trans. B* **2022**, *53*, 999–1017. [CrossRef]